Remote Sensing of Environment 285 (2023) 113374

Contents lists available at ScienceDirect

Remote Sensing of Environment

journal homepage: www.elsevier.com/locate/rse

A robust index to extract paddy fields in cloudy regions from SAR time series

Shuai Xu [a], Xiaolin Zhu [a,*], Jin Chen [b], Xuelin Zhu [c], Mingjie Duan [a], Bingwen Qiu [d], Luoma Wan [a], Xiaoyue Tan [a], Yi Nam Xu [a], Ruyin Cao [e]

[a] Department of Land Surveying and Geo-Informatics, The Hong Kong Polytechnic University, Hong Kong, China
[b] State Key Laboratory of Remote Sensing Science, Faculty of Geographical Science, Beijing Normal University, Beijing 100875, China
[c] Sichuan Tianfu New Area Vocational School, Chengdu 610000, Sichuan, China
[d] Key Laboratory of Spatial Data Mining & Information Sharing, Ministry of Education, Fuzhou University, Fuzhou 350116, Fujian, China
[e] School of Resources and Environment, University of Electronic Science and Technology of China, Chengdu, Sichuan 611731, China

ARTICLE INFO

Edited by Marie Weiss

Keywords:
Paddy rice
SAR
Sentinel-1
Mapping
Rice index
SPRI

ABSTRACT

Timely and accurate mapping of paddy rice cultivation is needed for maintaining sustainable rice production, ensuring food security, and monitoring water usage. Synthetic Aperture Radar (SAR) remote sensing plays an important role in the continuous monitoring and mapping of rice cultivation in cloudy regions since it is not affected by weather conditions. To date, most SAR imagery-based rice mapping methods rely on prior knowledge (e.g., the planting date) and empirical thresholds for specific regions, which limits their applications in large spatial scales. To tackle this limitation, this study proposed a new SAR-based Paddy Rice Index (SPRI) to quantify the probability of land patches planted paddy rice. SPRI fully uses unique features of paddy rice during the transplanting-vegetative period in the Sentinel-1 VH backscatter time series. With the assistance of cloud-free Sentinel-2 images, SPRI can be calculated for each cropland object with adaptive parameters. Then, SPRI values of cropland objects can be converted to paddy rice maps using the binary-classification threshold. The proposed SPRI method was tested at five sites with diverse climate conditions, landscape complexity and cropping systems. Results show that the SPRI was able to produce an accurate classification map with an overall accuracy of over 88% and an F1 score of over 0.86 at all sites. Compared with the existing SAR-based rice mapping methods, our method performed much better in heterogeneous agricultural areas where rice is mosaiced with other crops. As SPRI does not need any prior knowledge, reference samples and many predefined parameters, it has high flexibility and applicability to support paddy rice mapping in large areas, especially for cloudy regions where optical remote sensing data is often not available.

1. Introduction

As one of the most important staple foods in the world, paddy rice occupies 12% of the global grain sowing area and feeds more than half of the world's population (Food, 1994; Li et al., 2020; Lowder et al., 2016). Moreover, rice cropping has significant environmental impacts as it consumes water and emits greenhouse gases (Dong et al., 2016; Montzka et al., 2011; Tian et al., 2016). Therefore, monitoring rice cropping in a timely and efficient manner is essential not only for the food security of the world (Li et al., 2012) but also for environmental issues related to water use and climate change. Compared with traditional survey-based methods, the remote sensing approach is both time- and labor-efficient for large-scale and long-term rice mapping and monitoring (Chauhan et al., 2019; Dong et al., 2016; Weiss et al., 2020).

Two sources of remotely sensed data are widely used for rice mapping, namely optical and synthetic aperture radar (SAR) data (Adrian et al., 2021). Based on the unique spectral patterns of rice inundation and transplanting stages (Fig. 1 (a)), vegetation indices (e.g. Normalized Difference Vegetation Index (NDVI) and Enhanced Vegetation Index (EVI)) and water-related indices (Normalized Difference Water Index (NDWI) and Land Surface Water Index (LSWI)), both derived from optical data, were extensively collaborated in paddy field extraction (Xiao et al., 2002). Recent studies have shown the superiority of the combination of vegetation and water indices in large-scale rice mapping when

* Corresponding author at: The Hong Kong Polytechnic University, Room ZS621, Block Z, 181 Chatham Road South, Kowloon, Hong Kong, China.
E-mail address: xiaolin.zhu@polyu.edu.hk (X. Zhu).

https://doi.org/10.1016/j.rse.2022.113374
Received 7 May 2022; Received in revised form 6 November 2022; Accepted 18 November 2022
Available online 29 November 2022

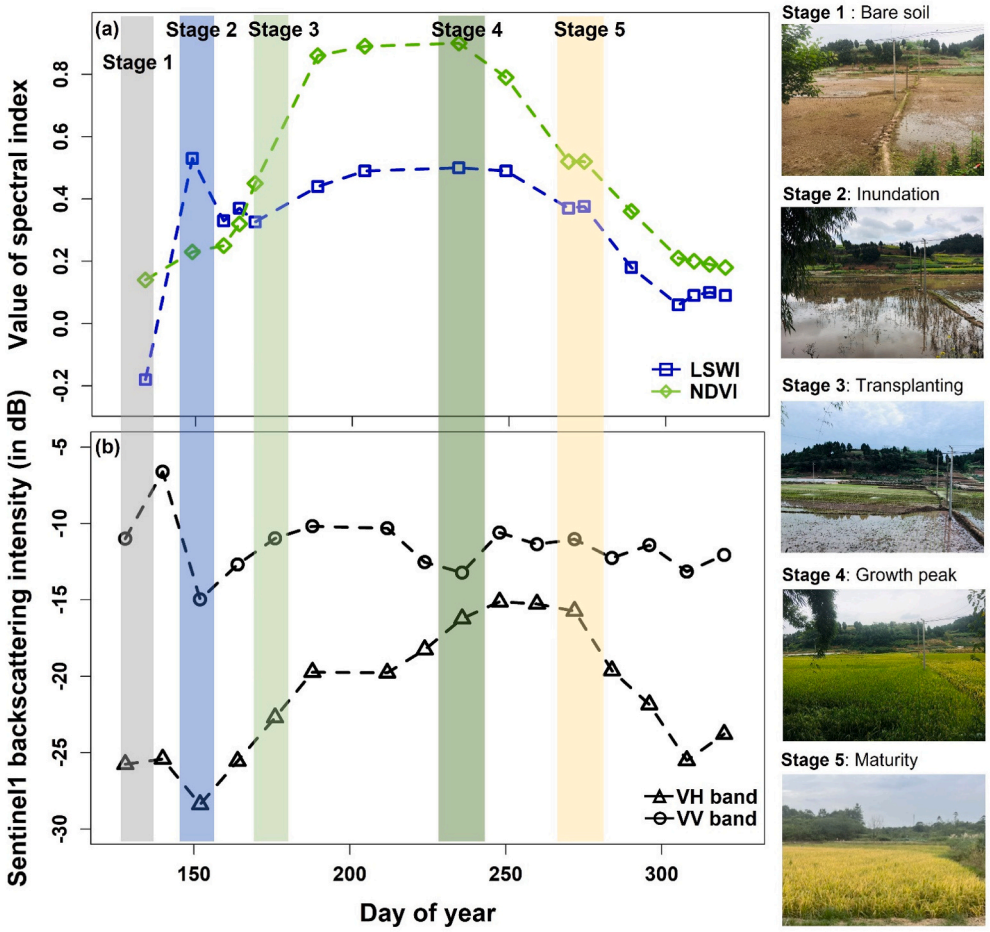

Fig. 1. Examples of LSWI and NDVI time series derived from Sentinel-2 images (a), Sentinel-1 VH and VV time series (b) during the rice growth period, and field photos of the key phenological stages of paddy rice (Photographed by Xuelin Zhu).

optical data are available at the critical growth stages (Dan et al., 2021; Qiu et al., 2015; Tornos et al., 2015). However, in practice, severe weather conditions limiting optical observations are usually present during these stages, especially in tropical and subtropical regions (Dong and Xiao, 2016; Motohka et al., 2009). As a result, SAR data has been increasingly used in recent years in cloudy regions, thanks to its capabilities to penetrate the cloud cover and reflect the electromagnetic and structural properties of ground targets (Chen et al., 2014; Clauss et al., 2018a, 2018b; Dong and Xiao, 2016).

Many studies have demonstrated that SAR time series can capture the signals of critical rice growth stages for rice mapping in cloudy regions (Canisius et al., 2018; He et al., 2018; Inoue et al., 2014; Li et al., 2020; Li and Bijker, 2019). The object-based classification approach is a promising method to identify paddy fields from SAR images (Gao et al., 2021; Park et al., 2018; Qi et al., 2017; Son et al., 2021; Yang et al., 2018). The most important reason is that it can mitigate the effect of the speckles in SAR images and improve the mapping accuracy (Jiao et al., 2014; Qi et al., 2017; Shah Hosseini et al., 2011; Xu et al., 2019). Besides traditional classifiers, deep-learning algorithms have been employed to map rice with various remote sensing data, including SAR time series (Lin et al., 2022; Pan et al., 2021; Thorp and Drajat, 2021; Wei et al., 2021, 2022; Xu et al., 2021). Driven by massive sample data, deep learning models can extract informative features automatically from SAR time series to get accurate paddy rice maps (Yang et al., 2022). In recent years, threshold-based methods are increasingly used for rice mapping in different regions and cropping systems (Bazzi et al., 2019; Li et al., 2020; Tian et al., 2018; Xie et al., 2015; Zhan et al., 2021). These threshold-based methods employ a hierarchical decision tree to combine the unique characteristics of rice. The pre-defined thresholds were applied to features associated with the "V"-shape pattern of backscattering during the rice growing cycle (see stages 2–4 in Fig. 1 (b)) (Chen et al., 2007; Clauss et al., 2018a; Nguyen et al., 2016; Pan et al., 2021; Zhan et al., 2021).

However, existing rice mapping methods using SAR images are not robust due to the following challenges. First, most studies require prior knowledge of rice phenology to define a time window for extracting phenology-related features, which limits the applicability of these methods in regions without prior knowledge (Dong and Xiao, 2016). Second, both classification and threshold-based methods need pre-training to ensure rice mapping accuracy. As a result, the performance of rice mapping largely depends on the availability and reliability of training samples, resulting in huge costs for large-scale applications (Fiorillo et al., 2020; Torbick et al., 2017). Third, the trained model in a local environment may not be applicable to other sites, as the large differences in the cropping system, rice phenology, terrain or any other factors may lead to differences in the intensity of SAR backscatter signal.

Besides classification and threshold-based methods, index-based methods are widely used to map target objects from remote sensing data, although it is rarely explored for mapping paddy rice from SAR time-series data. Compared with classification and threshold-based methods, index-based methods have two significant strengths: (1) it uses universal characteristics of the target objects so it has good applicability in different conditions; and (2) the index is a continuous variable correlated to the probability or coverage of the target objects, which can provide a more objective and flexible map of the target object than hard classifications. Various indices have been successfully developed to map

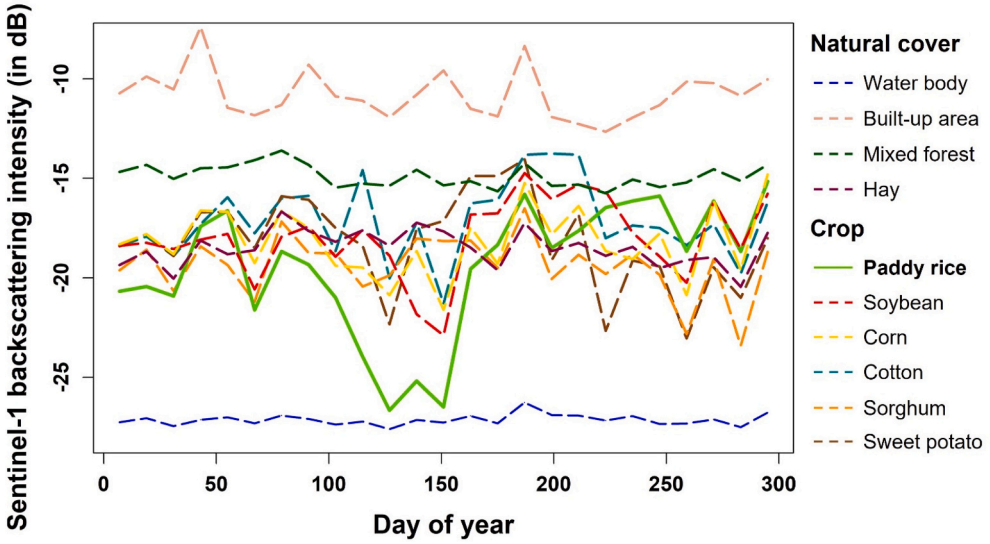

Fig. 2. Examples of Sentinel-1 VH time series of different land cover types and crops in this study.

different objects, such as the biological soil crust index (BSCI) (Chen et al., 2005), normalized difference yellowness index (NDYI) (Sulik and Long, 2016), and mountain green cover index (MGCI) (Bian et al., 2020). Therefore, developing a SAR-based rice mapping index to synthesize unique temporal backscatter patterns of rice growth could be a solution to overcome the limitations of existing studies.

Inspired by those index-based studies, we proposed a SAR-based Paddy Rice Index (SPRI) in this study for mapping paddy rice cultivation in cloudy regions. The proposed SPRI index could fulfill the following goals: 1) to enlarge the interclass difference while tolerating the intraclass variation of SAR signals; 2) to avoid the collection of large training samples and 3) to consider local conditions adaptively and achieve robust mapping results in different regions. The proposed SPRI index was calculated for each farming land object to generate the paddy rice maps. The land objects can be obtained from cloud-free Sentinel-2 optical images. The proposed method was tested at five sites in USA and China with diverse climate conditions, landscape complexity and cropping systems.

2. Development of a novel rice mapping index: SPRI

2.1. Temporal signature of sentinel-1 backscatters for different land cover types

SPRI was developed based on the feature analysis of the temporal signature of Sentinel- 1 VH backscatter for different land cover types as shown in Fig. 2, since VH is better than VV band for capturing the unique characteristic of rice growth as shown in Fig. 1 (b) and demonstrated by other studies (He et al., 2018). Generally, different land covers exhibit differences in the backscattering intensity and temporal variation given that SAR signals are sensitive to the electromagnetic and structural properties of land surface objects. Built-up areas typically generate strong backscattering which indicates the presence of dihedral structures formed by the building wall and ground. The water surface has very low backscattering intensity and is easy to separate from other land covers because the impinging radar energy is predominantly reflected away. For vegetation, its backscatter largely relies on the phenological stages during the growth period. Standing vegetation (e.g., mixed forest) shows a more stable temporal pattern than grassland which exhibits seasonal characteristics. Besides, crops have lower backscatter values and greater dynamic backscatter ranges than natural vegetation (Zhan et al., 2021). Crops tend to have higher backscattering intensity at the vegetative and maturity stages due to the rebound interaction among

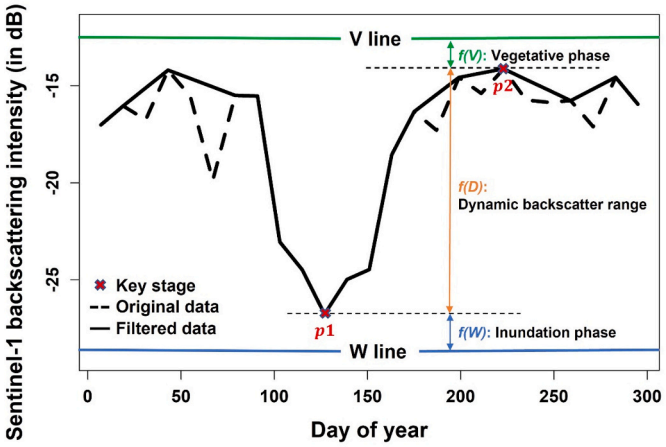

Fig. 3. Diagram of three features in the Sentinel-1 VH time series for designing the paddy rice index in Eq. (1). The solid line is smoothed Sentinel-1 VH time series and details of smoothing processing are described in Session 4.2.

vegetation components while the intensity is approximately equal to bare soil after harvest. Therefore, within-season temporal dynamics of backscatter during crop growth are often extracted by existing studies as key features for crop mapping and classification (Bazzi et al., 2019; Clauss et al., 2018a; Torbick et al., 2017).

As a semi-aquatic plant, paddy rice is the only major crop that has flooded fields during the initial stage. The backscattering mechanism of rice during the growth period is mainly affected by soil moisture, plant coverage and height. During the inundation period, the backscattering intensity is mainly affected by surface water since the plant is small and plant coverage is sparse (stage 2 in Fig. 1). As a result, the backscattering values of the transplanting stage are much lower compared with other vegetation or crops without irrigation (Fig. 2). By contrast, the backscatter intensity of rice exhibits no significant difference from other vegetation at the maturity stage (Fig. 2). The temporal variation of water–soil–vegetation composition that corresponds to backscattering intensities during stages 2–4 in Fig. 1 (b) are critical features in paddy rice identification.

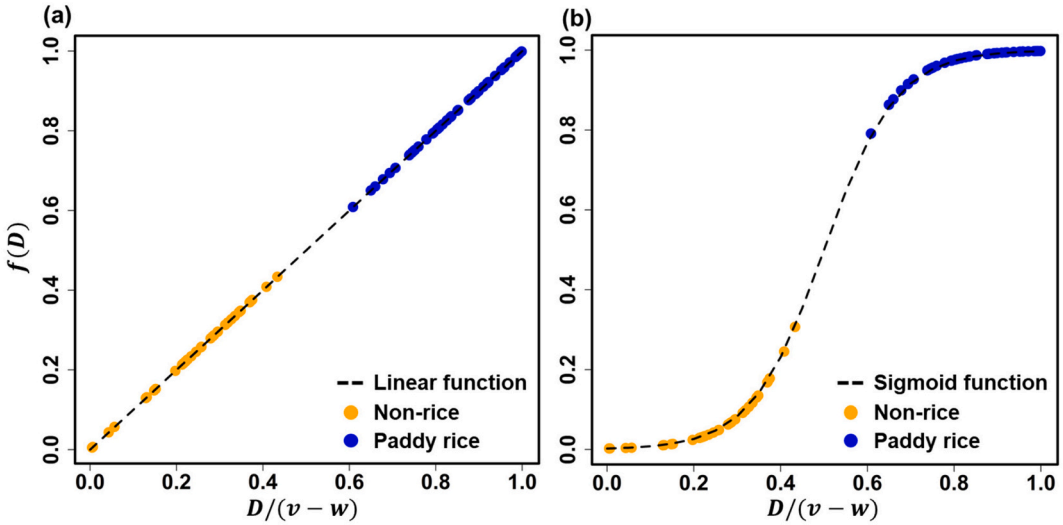

Fig. 4. Comparison of function *f*(*D*) values between paddy rice and other land covers using linear function (a) and sigmoid function (b).

2.2. SPRI design

Based on temporal pattern analysis of paddy rice compared with other land covers and crops in Section 2.1, the unique characteristics of rice growth can be summarized as the large range of backscatter dynamics during the growing period that is greater than other crops (characteristic 1); low backscatter value at the inundation stage that is close to that of water (characteristic 2); and high volume-scattering characteristic at the vegetative stage that is close to that of other vegetation (characteristic 3). To quantify these characteristics, a Vegetation-Water zone was defined by setting up an upper boundary to represent the maximum intensity (*v*) of local vegetation (hereinafter referred to as "V line") and a lower boundary to denote the intensity (*w*) of local water surface (hereinafter referred to as "W line") (Fig. 3). Then, three

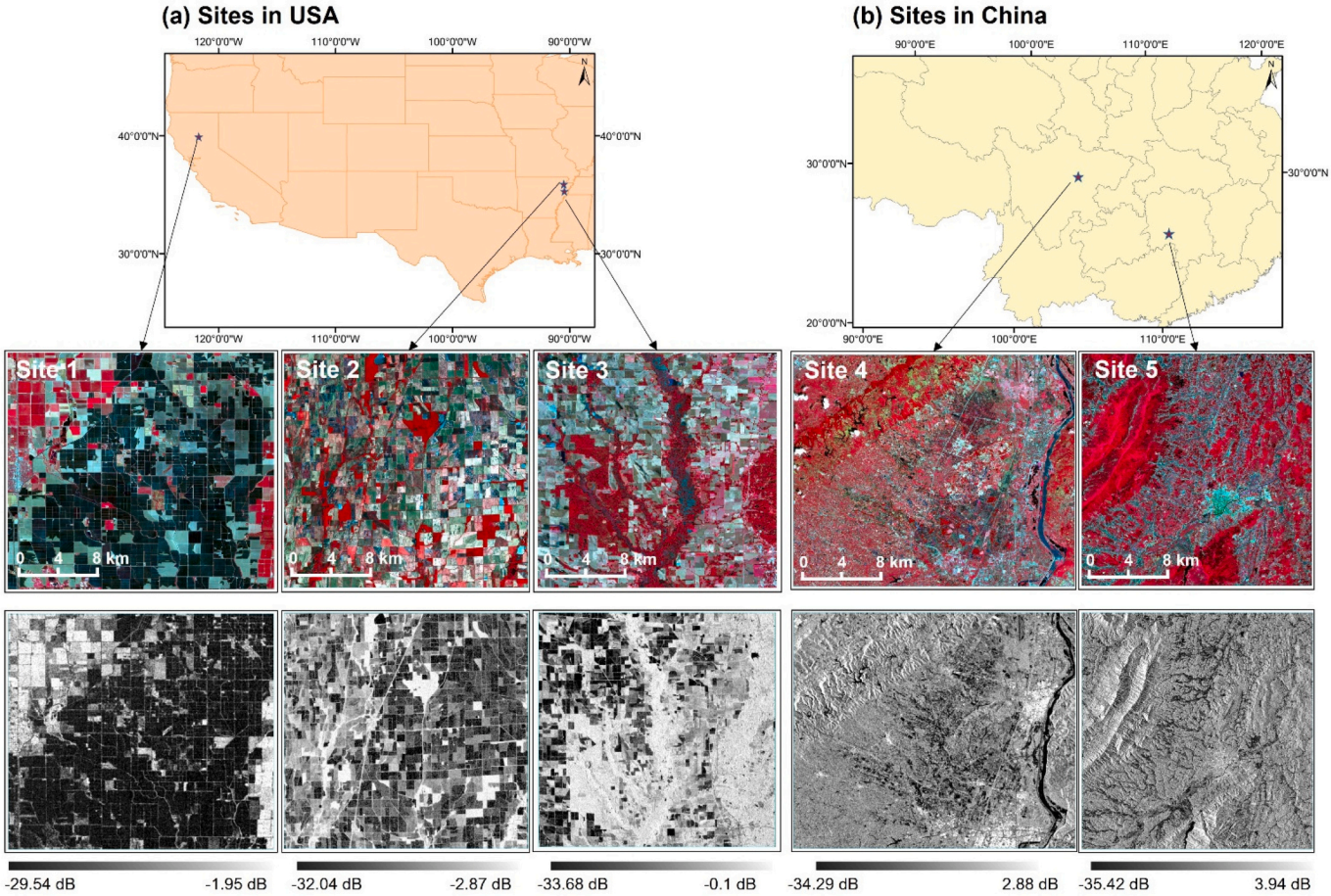

Fig. 5. Location of five selected sites in the USA (a) and China (b) used in this study (upper row) and false-color compositions of cloud-free Sentinel-2 images (middle row) and Sentinel-1 VH image (bottom row) near the transplanting stage.

measurements, $f(D)$, $f(W)$, and $f(V)$, were developed to quantify the three characteristics respectively in the growth period of paddy rice (from point $p1$ to $p2$ in Fig. 3). $f(D)$ measures the closeness of the backscatter dynamic range of a given crop field close to that of a rice field, $f(W)$ quantifies the similarity of the local minimal intensity during the growth period with local water, and $f(V)$ quantifies the similarity of the local maximal intensity during the growth period with local vegetation, respectively. Paddy rice should hold all three characteristics simultaneously. Therefore, SPRI was designed to integrate all three measurements as Eq. (1):

$$SPRI = f(D) \times f(W) \times f(V) \tag{1}$$

Theoretically, $f(D)$ can be calculated as the ratio between backscatter range D (i.e., $p2$ - $p1$) and the depth of the V—W zone (i.e., v - w), i.e., $f(D) = D/(v - w)$, which is a simple linear function to rescale the value of D to 0–1 for quantifying the probability of paddy rice. However, this simple linear function cannot well differentiate paddy rice and other crops (Fig. 4 (a)). To enlarge the difference between paddy rice and other crops, $f(D)$ uses a sigmoid function to rescale the value of D to 0–1 (Fig. 4 (b)) as Eq. (2):

$$f(D) = \frac{1}{1 + e^{\left(\frac{v-w}{2} - D\right)}}, D = p2 - p1 \tag{2}$$

where v and w represent the backscatter intensity of V line and W line respectively, and $p1$ and $p2$ are the local minimal and maximal intensity during the growth period respectively. D, v, w, $p2$ and $p1$ are with unit dB. Values of v, w, $p1$, and $p2$ are all extracted from SAR time series (details in Session 4.2).

For $f(W)$, the quadratic function as Eq. (3) was employed to convert the relative difference between $p1$ and W line (*i.e.*, $W = \frac{p1-w}{v-w}$) to a closeness measurement ranging from 0 to 1 to represent the probability of paddy rice, and meanwhile, enlarge the difference between paddy rice and other land covers by the square operation. Similarly, Eq. (4) is used for $f(V)$ to measure the closeness of $p2$ to the V line.

$$f(W) = 1 - W^2, W = \begin{cases} 1, p1 \geq v \\ \dfrac{p1 - w}{v - w}, w \leq p1 < v \\ 0, p1 < w \end{cases} \tag{3}$$

$$f(V) = 1 - V^2, V = \begin{cases} 1, p2 \leq w \\ \dfrac{v - p2}{v - w}, w < p2 \leq v \\ 0, p2 > v \end{cases} \tag{4}$$

Finally, for $f(D)$, $f(W)$, and $f(V)$, all of them range from 0 to 1 and they exhibit the same direction, where the large values suggest a high probability of paddy rice cultivation. As a result, their integration by Eq. (1) also ranges from 0 to 1 and large values suggest a high probability of paddy rice cultivation. The combination of three measurements can give a more robust estimation of the probability of paddy rice cultivation than using a single measurement. These three components are combined by multiplication, because they all are necessary conditions for judging a cropland object as rice cultivation. Using multiplication rather than addition is to ensure that a land patch is classified as paddy rice only if it has all three characteristics simultaneously. If they were combined by addition, one of the components would be ignored if other two components dominate. For example, some water-intensive crops with a relatively large value of $f(D)$ and $f(V)$ would be misclassified as paddy rice if using addition formula (see examples of rice and soybean in Appendix A. Supplementary Data).

Table 1
Summary of rice planting information at five study sites.

Study site	Rice type	Ratio of rice field to total cropland	Average size of rice objects (acre)	Rice growth period
Site 1	Single rice	62%	78.6	May to September
Site 2	Single rice	42%	41	May to September
Site 3	Single rice	21%	41	May to September
Site 4	Single rice	38.5%	7.4	May to August
Site 5	Single/ double rice	80%	7.8	Single: May to August Double: March to July/July to October

3. Study area and data

3.1. Study area

Five sites were selected as the study area (Fig. 5) that have differences in 1) geographical and climate conditions; 2) landscape complexity; and 3) cropping systems (Table 1). The sites 1–3 located in the USA are the region of intensive agriculture, where the cropland is the main land use type. Site 1 is located in the Glenn County, California State (122°0′–122°12′W and 39°26′–39°36′N) with an average temperature of 16.01 °C and annual precipitation of around 600 mm. Dense rice fields are a big part of the agricultural base of Glenn County. Sites 2 and 3 are both located in the Mississippi River basin, where the watershed is dominated by agriculture. Site 2 is located in Poinsett County, Arkansas (90°42′–91°06′W and 35°22′–35°37′N), with 1270 mm annual precipitation and 15.89 °C temperature on average. Paddy rice, soybean, corn, and potatoes are the main grain crops at site 2, while their distribution is mixed. Most fields yield one-season crops and they share a similar crop calendar. Therefore, site 2 is capable to assess the performance of rice extraction under the scenario of heterogeneous crop distribution. Site 3 overlaps with the Cross County and St. Francis County, Arkansas (90°36′–91°06′W and 34°55′–35°21′N) and has the similar crop types and cropping systems to site 2, whereas croplands are mixed distributed with woody wetlands and forests. The experiment at site 3 can reveal the influence of natural vegetation on rice field recognition, especially the influence of wetlands where the soil is periodically dabbled or covered by water.

Sites 4 and 5 are located in the mountainous region of Sichuan and Hunan provinces in China, respectively, where the distinctive agricultural characteristic is smallholder farming. Site 4 is located in Meishan City, the south-western part of Chengdu Plain and the conjunction between Chengdu Plain and Hengduan Mountains (103°37′–103°54′E and 30°3′–30°16′N). Its altitude is higher in the west and lower in the east with a gentle slope inclination. Site 4 has a subtropical monsoon climate, with an average annual precipitation of 1000–1500 mm and temperatures ranging from 6 °C in January to 25 °C in August, and the sky is constantly cloudy and rainy for most of the growing period. Site 5 is located in the hilly area of Wugang City (110°26′–110°45′E and 26°37′–26°56′N), Hunan province with an average annual precipitation of 1200 mm, and an average temperature of 16.8 °C. Rice is the main grain crop in the whole site and is cultivated on the lower land. Sites 4 and 5 are selected to assess the rice mapping capacity in cloudy regions with mountainous terrain and smallholder farming system. Detailed rice planting information of five sites is listed in Table 1.

3.2. Sentinel-1 and Sentinel-2 data

Sentinel-1 is one of the most widely used radar satellites which is the first of the Copernicus Program satellite conducted by the European Space Agency. The instrument has a swath of up to 400 km. The satellite is on a sun-synchronous, near-polar (98.18°) orbit with a 12-day repeat

Table 2
Summary of Sentinel-1 time series used in this study.

Study site	Country	Orbit	Incidence angle (°)	Path	Frame	Acquisition period
Site 1	USA	Ascending	30.47–31.55	137	124	Jan.05 – Dec.30, 2020
Site 2	USA	Ascending	38.31–39.87	165	110	Jan.07 – Dec.20, 2020
Site 3	USA	Ascending	38.10–39.88	165	110	Jan.07 – Dec.20, 2020
Site 4	China	Ascending	39.57–40.31	128	94	Feb.12 - Dec.21, 2017
Site 5	China	Ascending	39.01–40.99	84	80&85	Jan.07 - Oct.22, 2021

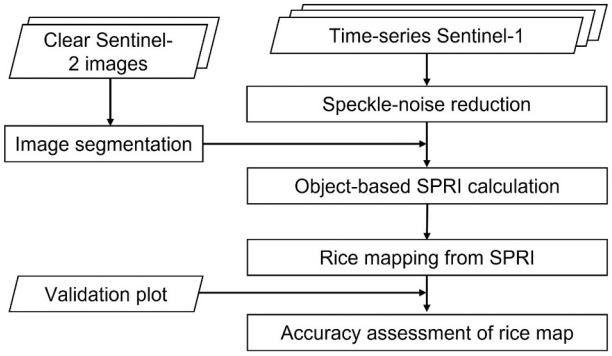

Fig. 6. The flowchart of mapping paddy rice using the SPRI method.

cycle. In this study, Sentinel-1 Ground Range Detected (GRD) scenes, a calibrated and ortho-corrected product provided by the Google Earth Engine (GEE), were used to generate SAR VH time series with 10 m spatial resolution and 12-day temporal resolution (Table 2). Such temporal resolution is promising for the monitoring of the growing stages of paddy rice (He et al., 2018). The acquisition periods of these SAR data are aligned with the date of sample data collection.

Auxiliary data involved cloud-free Sentinel-2 images (e.g., cloud coverage <10%) and annual spectral index composite for study sites. To achieve a good spatial consistency with Sentinel-1 images, only the bands with 10 m resolution within Sentinel-2 images (blue, green, red and near-infrared bands) were obtained from the GEE platform. Besides, two spectral indices, namely, NDVI and NDWI, were derived to reflect land cover information of vegetation and waterbody, respectively. The annual maximum NDVI and NDWI (hereinafter referred to as "NDVImax" and "NDWImax") were also calculated based on all available Sentinel-2 images within one year to reduce the influence of cloud contamination.

4. Mapping paddy rice cultivation based on SPRI

The workflow of rice mapping in cloudy regions using the developed SPRI index is shown in Fig. 6, including four major steps after the preprocessing step of speckle-noise reduction by a 7 × 7 refined Lee-Sigma filter (Lee et al., 1999). In this study, the SPRI calculation is implemented on the entire region to make the whole process simple and automatic, but it can be applied to only croplands if a map of croplands is available. First, based on cloud-free Sentinel-2 images, image segmentation was implemented to generate homogeneous land parcels. Second, we calculated the SPRI value for segmented objects to quantify the probability of land patches planted paddy rice. Third, the object-based SPRI values were classified by a threshold to obtain rice maps. Last, the accuracy of rice maps derived from SPRI was further assessed by validation samples at five sites and compared with existing rice mapping methods.

4.1. Sentinel-2 image segmentation

The object-based approach has been widely used to reduce the noisy effect in land cover classification over agriculture areas with geometric features, such as the crop field boundary (De Castro et al., 2018; Lebourgeois et al., 2017; Li et al., 2015; Peña-Barragán et al., 2011). In this study, the combination of Canny edge detection and watershed segmentation, referred to as the CEWS workflow (Watkins and van Niekerk, 2019a, 2019b), was applied for field boundary delineation, due to its robustness and transferability in diverse agricultural systems (Watkins and van Niekerk, 2019a, 2019b).

First, edge images for each band of each Sentinel-2 image were generated by the Canny algorithm which was implemented in R using the 'imager' package (version 0.42.11). The adjustable parameter, *alpha,* of which a large parameter tends to detect strong edges and a lower parameter may include some weak edges (default 1.0), was set as 1.0 for three sites in the USA and 0.8 for two sites in China. Next, the *Z*-score

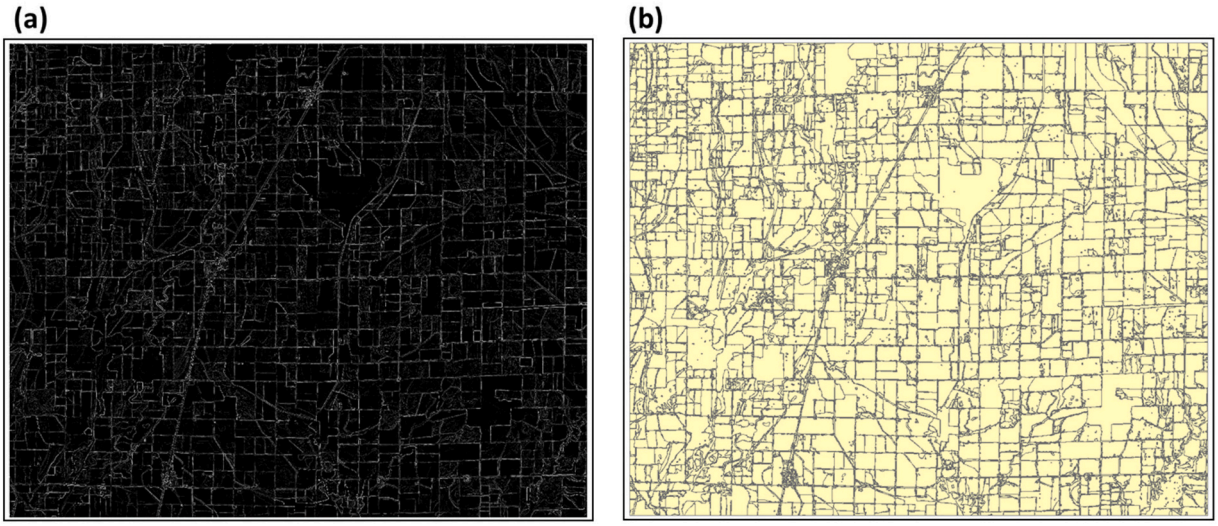

Fig. 7. Results of Canny edge detection (a) and results of watershed segmentation (b) for site 2.

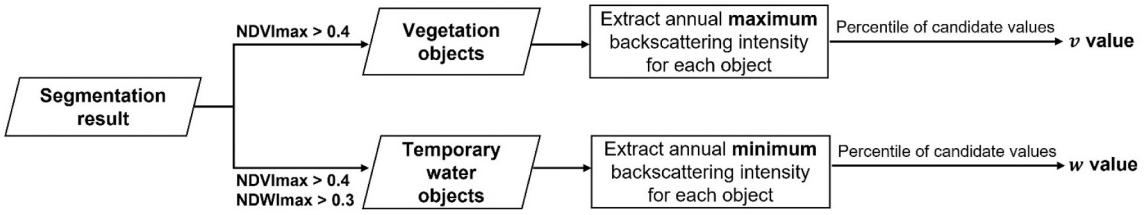

Fig. 8. The workflow of ***w*** and ***v*** determination for study sites.

Table 3
Summary of parameter *w* and *v* used for SPRI calculation at five study sites.

	Parameter *w*		Parameter *v*	
	Percentile	Value	Percentile	Value
Site 1	10% Percentile	−26.48	10% Percentile	−18.02
Site 2	10% Percentile	−31.82	10% Percentile	−16.16
Site 3	10% Percentile	−31.42	10% Percentile	−15.82
Site 4	75% Percentile	−22.65	25% Percentile	−14.85
Site 5	75% Percentile	−23.57	25% Percentile	−15.30

algorithm, followed by a max-min normalization was employed to standardize the composite edge layer used for image segmentation (Fig. 7 (a)). To avoid the influence of noise, the layer values were divided into five classes from smallest to largest using the Jenks' natural breaks (JNB) algorithm (Jenks, 1967) and the value belonging to the first class was abandoned. Then, the watershed algorithm (Fig. 7 (b)) was used to segment the aggregated edge layer because it is sensitive to weak edges and is guaranteed to obtain closed continuous edges (Shafarenko et al., 1997). Since watershed segmentation is prone to produce a large number of small objects (Bleau and Leon, 2000), tiny objects (i.e., size <10 pixels) were filtered out in the segmentation results considering that they are unlikely to be cropland parcels. Finally, objects of land parcels at each site were obtained for the object-based SPRI calculation.

4.2. Object-based SPRI calculation

For each image object, two parameters are required for SPRI calculation, including the backscattering intensity of the W line and V line (i.e., *w* and *v* in Eqs. (2)–(4)). Different study sites would have different *w* and *v* due to different land surface structures and other factors such as orbit geometry. Therefore, adaptive *w* and *v* values with consideration of site differences are necessary when calculating SPRI.

The two parameters can be determined by the backscattering intensity of local vegetation and temporary water objects (i.e., flooded rice fields during the inundation stage) using the workflow in Fig. 8. Specifically, NDVImax and NDWImax were firstly used to select vegetation and temporary water objects respectively, using a threshold approach. NDVI >0.4 is generally viewed as vegetation coverage (Peng et al., 2019), and NDWI >0.3 is usually for the detectable water surface (McFeeters, 2013). Thus, vegetation objects (NDVImax >0.4) and temporary water objects (NDVImax >0.4 and NDWImax >0.3) within each site can be identified. Then, the annual maximum backscattering intensities of each vegetation object and minimum backscattering intensities of each water object can be calculated. Finally, the *v* and *w* values were determined with a percentile strategy. The parameters of *w* and *v* determined for each site are shown in Table 3, which was based the sensitivity analysis in sites with different terrains, i.e., flat or hilly (see details in Section 6.2).

In addition, local minimal and maximal points ($p1, p2$) are needed to be extracted from the Sentinel-1 time series to compute SPRI, which can be automatically accomplished by seeking turning points in the Sentinel-1 time-series curve (e.g., the gradient of the curve to be zero). The details of turning point extracting steps can be found in Appendix A. Supplementary Data. Ideally, each pair of $p1$ and $p2$ represents a rice growing period. However, unintended pairs of $p1$ and $p2$ can be found due to rainfall events which cause a short-term drop in backscattering intensity. By assuming that the rice growing cycle is much longer than rainfall events, the drops shorter than 40 days in the Sentinel-1 time series were filtered out by linear interpolation (see original and filtered Sentinel-1 time series in Fig. 3) (Asilo et al., 2014; Zhu et al., 2008). Finally, reliable local minimal and maximal points ($p1$, $p2$) and their backscattering intensity were extracted from the filtered Sentinel-1 time series. It is worth noting that multiple pairs of local maximal and minimal points may be obtained from Sentinel-1 time series of one year due to multi-season cropping practice. All pairs were put into Eq. (1) for

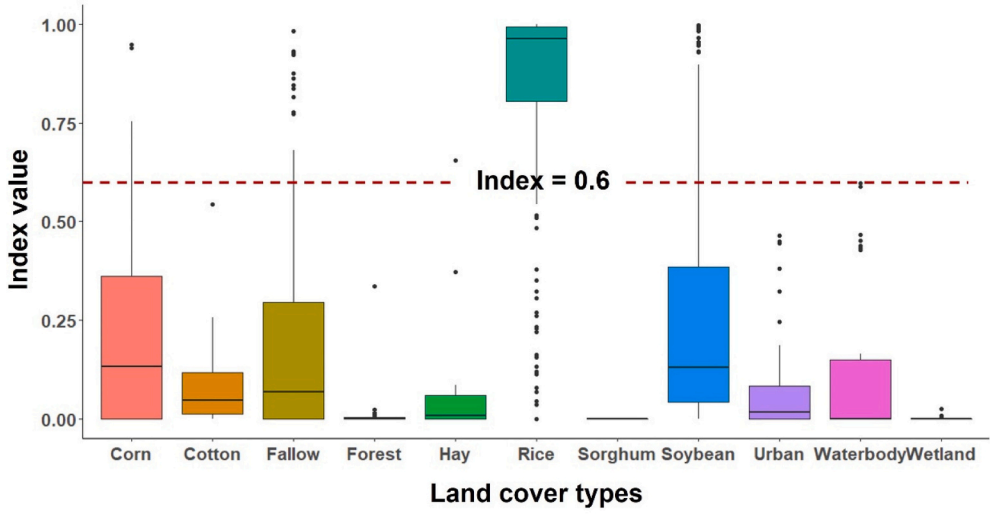

Fig. 9. The box plot of the calculated index value of land cover types at Site 3.

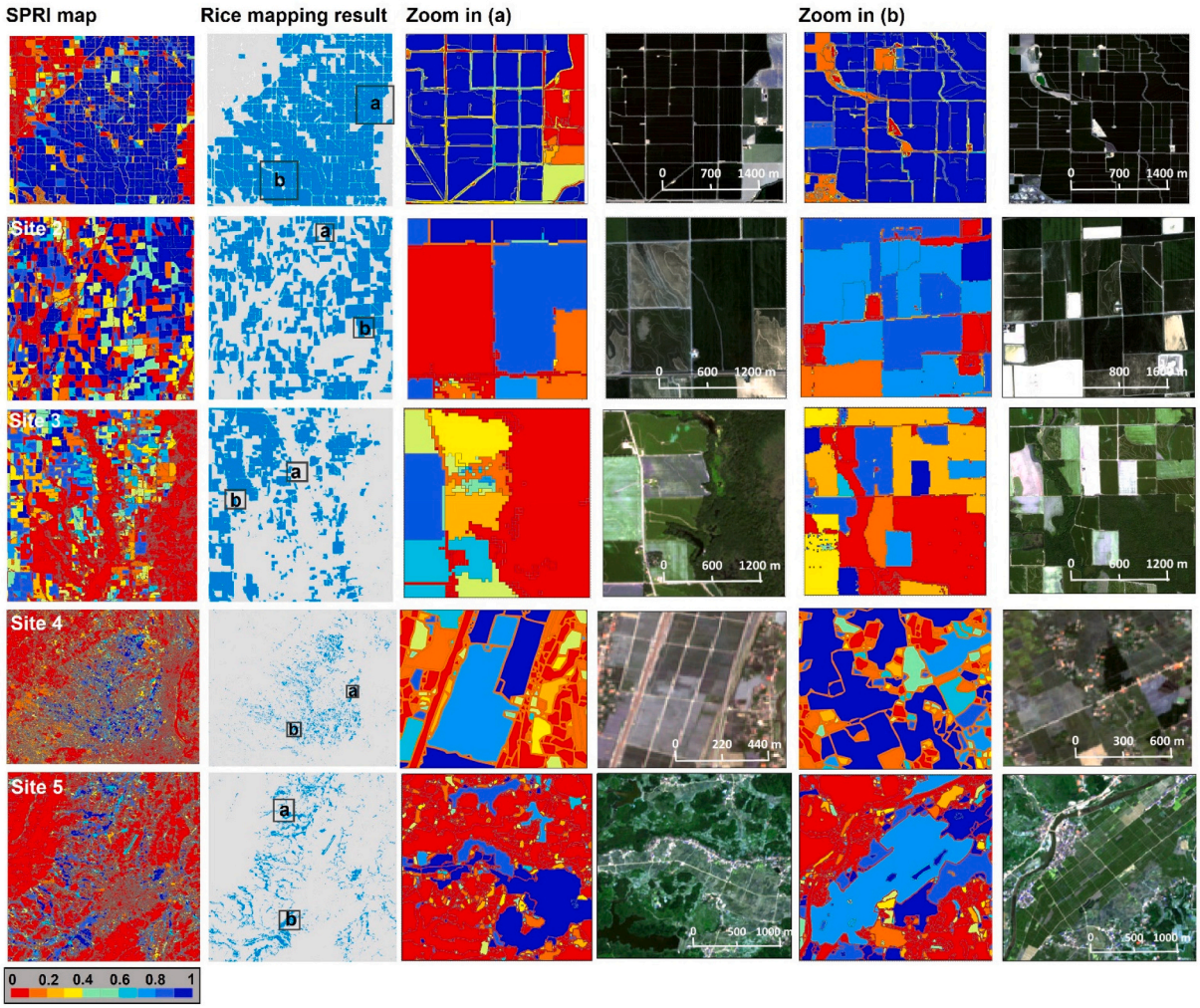

Fig. 10. The SPRI map (first column) and derived rice maps (second column) at the five study sites, and SPRI maps and true-color Sentinel-2 images of the zoomed sub-region (a) (third and fourth column) and sub-region (b) (fifth and sixth column) in each site.

computing SPRI values.

4.3. Rice mapping from SPRI by binary-classification

SPRI value indicates the probability of a land parcel being planted with paddy rice. As a result, it can be used to classify each object into paddy rice and non-rice by an appropriate threshold. Since SPRI has already normalized the differences caused by different sites to a large extent, a uniform threshold can be used for mapping paddy rice at different sites. To determine this threshold, SPRI values of different land cover types and crops at site 3 were summarized by box plots (Fig. 9) because site 3 has more different land cover types than other sites. As shown in the box plots in Fig. 9, SPRI values of paddy rice are much higher than other land cover types except for few outliers. Finally, we determined the threshold as 0.6 for classifying SPRI values into the rice and non-rice classes. More discussions about the selection of threshold were in Section 6.2.

4.4. Accuracy assessment and performance comparison

4.4.1. Validation plot

Validation sample sets for sites 1–3 were collected from the United States Department of Agriculture (USDA) Cropland Data Layer (CDL) with 30 m spatial resolution (https://nassgeodata.gmu.edu/CropScape/). USDA CDL was produced using the machine learning method, in situ reference data, and multi-date satellite images to identify >100 crop types (Johnson and Mueller, 2010). High classification accuracies (>90%) for major crop types were reported (Boryan et al., 2011) and numerous agriculture-related studies and land cover change studies have employed the CDL dataset as reference data (Diao et al., 2021; Johnson and Mueller, 2021; Park et al., 2018; Wu et al., 2021). In this study, we manually checked the CDL maps over three sites with the support of Google Earth and generated a 10 m binary classification map of rice and non-rice using the nearest neighbor resampling method (see reference maps in Fig. 11). Validation sample sets of the sites 4 and 5 in China were ground survey samples collected in 2016 (site 4) and 2021 (site 5) respectively. Site 4 has 30 rice cultivation samples and 30 non-rice samples, while site 5 has 53 rice cultivation samples and 50 non-rice samples. Each sample was at least 50 m wide and 50 m long to match the scale of remote sensing data (He et al., 2018). A hand-held GPS unit was used to locate the samples, which were projected to the radar data.

4.4.2. Accuracy metrics

The validation samples were used to calculate the accuracy of the rice mapping. Since the sample size of sites 4 and 5 is limited, we combined validation samples of these two sites with a total of 83 rice plots and 80 non-rice plots. The producer's accuracy (PA), user's accuracy (UA), overall accuracy (OA), and F1 score (Hripcsak and Rothschild, 2005) were adopted to assess the rice mapping accuracy. These accuracy measures were calculated using the equations (Eqs. (5)–(8)):

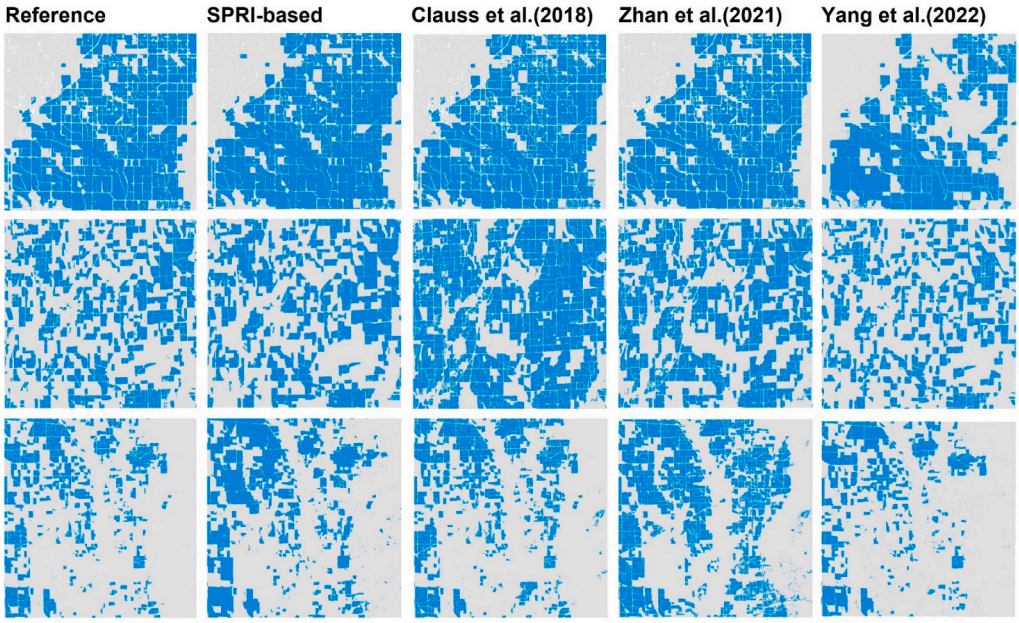

Fig. 11. Comparison of rice mapping results obtained with four methods in site 1(upper row), site 2 (middle row), and site 3 (lower row).

$$PA = \frac{x_R}{x_{i*}} \tag{5}$$

$$UA = \frac{x_R}{x_{*j}} \tag{6}$$

$$OA = \frac{Sd}{n} \tag{7}$$

$$F1\ score = \frac{2 \times UA \times PA}{UA + PA} \tag{8}$$

where x_R is the number of samples with true rice cover that is classified as rice by the algorithm, x_{i*} represents the total number of samples that are classified as rice, and x_{*j} represents the total number of samples with true rice cover. Sd is the number of samples that are correctly classified, and n denotes the total number of validation samples.

We compared the performance of rice mapping based on SPRI with other two rule-based rice mapping methods and one deep learning-based method at all study sites. For the rule-based methods, two methods developed by Clauss et al. (2018a, 2018b) and Zhan et al. (2021) were selected for comparison because they are the most recent studies and attracted more attention with a large number of citations. Both methods use the dynamic range of SAR backscatter during the rice growing period as the key feature for rice identification with predefined thresholds. Values of these thresholds reported in Clauss et al. (2018a, 2018b) and Zhan et al. (2021) were employed for rice mapping at the five sites. For the deep learning-based method, the temporal feature-based segmentation (TFBS) model (Yang et al., 2022) developed recently was selected for comparison. It integrated the LSTM and UNET module to extract temporal and spatial features for rice mapping with time-series SAR images and obtained a better result than the model of LSTM, UNET, and convolutional LSTM. We trained the TFBS model using the samples in USA shared by its developer (Yang et al., 2022) and applied the trained model to our five sites. Since our method was assessed at the object scale, for fairness of comparison, the two rule-based methods were applied to objects from image segmentation, and the pixel-wise result from TFBS was further aggregated to objects by using majority rule.

5. Results

5.1. SPRI values

SPRI values for five sites are shown in Fig. 10 (the first column). It shows that the high SPRI values (blue objects) well agree with the inundated areas in Sentinel-2 images (dark areas of the zoomed true-color Sentinel-2 images in Fig. 10). These inundated areas indicate the flooded stage of the rice planting practice. Besides, we can see that low SPRI values (red objects) match with the areas of natural vegetation and other land covers. Objects with moderate SPRI values are rare at all sites, suggesting that SPRI values can well distinguish rice from non-rice covers. Furthermore, histograms of SPRI values of three USA sites and two Chinese sites show a similar by-modal pattern (see the first column in Fig. 14), although land conditions and climate background are different between the two countries. It is clear that this by-modal histogram is a combination of rice and no-rice classes, confirming that SPRI successfully enlarges the difference between rice and other non-rice covers. Fig. 10 also shows variability in SPRI values for paddy rice fields (e.g., light blue to dark blue cover in the SPRI maps), which may be caused by the biophysical factors (e.g., different seeding density) and environmental factors (e.g., irrigation conditions).

5.2. Classification map of rice cultivation and accuracy assessment

Maps of rice cultivated areas at five sites based on SPRI values are shown in Fig. 10 (second column). Rice maps at all sites were generated by classifying the SPRI image using threshold 0.6 which was explained in Section 4.3. The visual comparison of paddy rice maps from SPRI segmentation and reference was presented for three sites in the USA. The classification maps of these three sites are visually similar with the reference maps (the first column in Fig. 11). Site 1 has the highest consistency, where rice cultivation occupied the major lands. For the other two sites where rice fields spatially were mosaiced with other croplands, more classification errors were observed than in site 1. For instance, some objects of natural vegetation were wrongly classified as rice in the western areas of site 2. Rice at two sites in China is mostly distributed in the flat valleys in these mountainous areas (Fig. 10). The zoom-in regions of sites 4 and 5 show the rice objects overlaying with the Sentinel-2 images, demonstrating a good delineation of rice fields

Table 4
Accuracy assessment of rice mapping: overall accuracy (OA), user's accuracy (UA), producer's accuracy (PA), and F1 score. UA, PA, and F1 score are for the rice class.

Study site	Sample size (rice: non-rice)	OA	UA	PA	F1 score
Site 1	486:187	0.95	0.96	0.98	0.97
Site 2	244:367	0.88	0.82	0.91	0.86
Site 3	229:513	0.94	0.90	0.91	0.91
Sites 4 and 5	83:80	0.91	0.90	0.92	0.91

Table 5
Accuracy assessment of four methods: user's accuracy (UA) and producer's accuracy (PA) for the rice class.

Study site	Accuracy	Index method	Rule-based method		Deep-learning method
		SPRI-based method	Clauss et al. (2018a, 2018b)	Zhan et al. (2021)	Yang et al. (2022)
Site 1	UA	0.96	0.95	0.94	0.99
	PA	0.98	0.93	0.93	0.7
Site 2	UA	0.82	0.56	0.65	1.00
	PA	0.91	0.98	0.93	0.90
Site 3	UA	0.90	0.48	0.50	0.94
	PA	0.91	1.00	0.91	0.93
Sites 4 and 5	UA	0.90	0.91	0.89	0.78
	PA	0.92	0.81	0.88	0.47

from other land covers (e.g., roads in site 4) in complex landscapes.

The accuracy assessment was performed for sites 1–3 individually. Sites 4 and 5 were combined to evaluate the accuracy because of the limited samples and their high similarity in terrain. High mapping accuracies were achieved, with an OA larger than or equal to 0.88 at all study sites (Table 4). We mapped paddy rice areas with the F1 score ranging from 0.86 at site 2 to 0.97 at site 1, indicating that the proposed method keeps the balance between the UA and PA. The PA for our target class, paddy rice, was greater than or equal to 0.91 at five sites, suggesting that our method has successfully identified the majority of the paddy rice objects at all sites. Different from PA, UA reflects the capacity of the proposed method to distinguish paddy rice and other land covers which may bring difficulties in rice mapping. UA reaches 0.9 except for site 2 (0.82). This may be because rice at site 2 is more mosaiced with other crops. Hence, the irrigation process may affect land parcels close to the rice fields, bringing challenges for differentiating rice from nearby other crops.

5.3. Comparison with existing rice mapping methods

Visual comparison between the proposed method and three existing methods at sites 1–3 shows that the map produced by our method is generally more similar with the reference map than other three methods (Fig. 11). We compared UA and PA of four methods among five study sites and found that our method can generally better balance omission and commission errors as results of our method show a higher UA and comparable PA compared with other methods (Table 5). At site 1, SPRI method and other two threshold methods perform well with satisfied PA and UA, proving their capacity for rice mapping in the region where rice is the dominant crop. However, the deep learning-based method obtained a PA value only 0.7, suggesting it missed many rice fields in a site where rice is the dominant crop. For sites 2 and 3, SPRI method and the deep learning-based method can get satisfied PA and UA values, but the two rule-based methods have very low UA values indicating that they misclassified many non-rice fields as rice in these two sites where rice is not a dominant crop. Specifically, SPRI method improved UA values of the two rule-based methods by 0.26 and 0.17 in site 2, 0.42 and 0.4 in site 3, respectively. It suggests that SPRI method can reduce the classification confusion by enlarging the differences between rice and other land covers, which is the big challenge when rice is mixed with other crops such as sites 2 and 3. For sites 4 and 5 in China, SPRI method and two threshold-based methods performed better than deep learning-based method, demonstrating the challenges of applying deep learning methods to regions without available training samples.

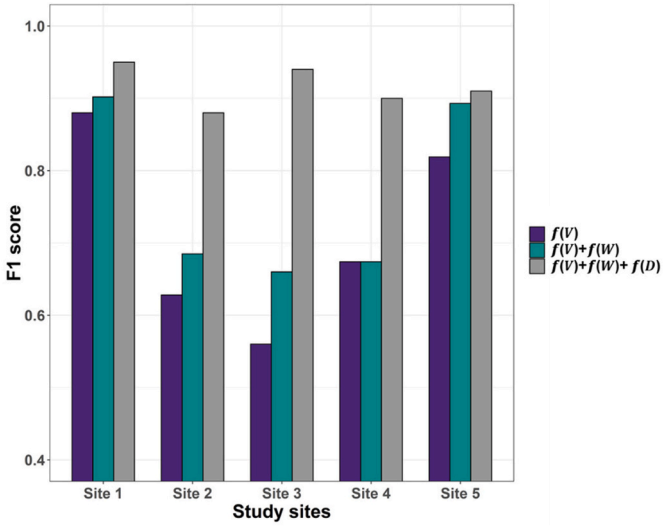

Fig. 12. Comparison of the rice mapping accuracy (F1 score) among the three scenarios using an ablation experiment for all sites.

6. Discussion

6.1. Advantages of SPRI

In this study, we introduced a new rice mapping index SPRI using Sentinel-1 time series and demonstrated its performance over five complementary sites with differences in climate background, terrain condition, and cropping system. It obtained good accuracies among five sites, mainly due to two advantages compared with existing methods.

First, the proposed index integrated three key rice growing features into one quantity for estimating the probability of rice cultivation over different regions, while existing methods only use part of these features or use them independently. For example, Nguyen et al. (2016) only employed local maximum value and backscatter amplitude as the static threshold of the decision tree, resulting in confusion with non-rice vegetation. To investigate the benefit of combining three features, an ablation experiment was used to illustrate the contribution of three features ($f(V)$, $f(W)$, and $f(D)$) to the improvement of rice mapping accuracy (Fig. 12). It shows that the integration of three features can get the highest F1 score for all sites, which is significantly better than using $f(V)$ and $f(W)$ or only $f(V)$ in three of the five sites. To better understand the results from the ablation experiment, values of three features of different crops and land covers were visualized in a three-dimensional plot (Fig. 13). It clearly shows the effectiveness of three components in distinguishing paddy rice from other crops and land covers. Rice mainly distributes on the right upper corner with high values of three components, while other non-rice land covers do not have large values (i.e., close to 1) of three sub-indexes concurrently. Therefore, the SPRI value from the multiplication of three sub-indexes can enlarge differences between rice and non-rice fields (an example of SPRI difference between rice and soybean can be found in Appendix A. Supplementary Data), thereby achieving the highest F1 score for all sites.

Second, the proposed method can enlarge the differences between paddy rice and other land covers by a non-linear rescaling for all features, which is different from the existing methods using original

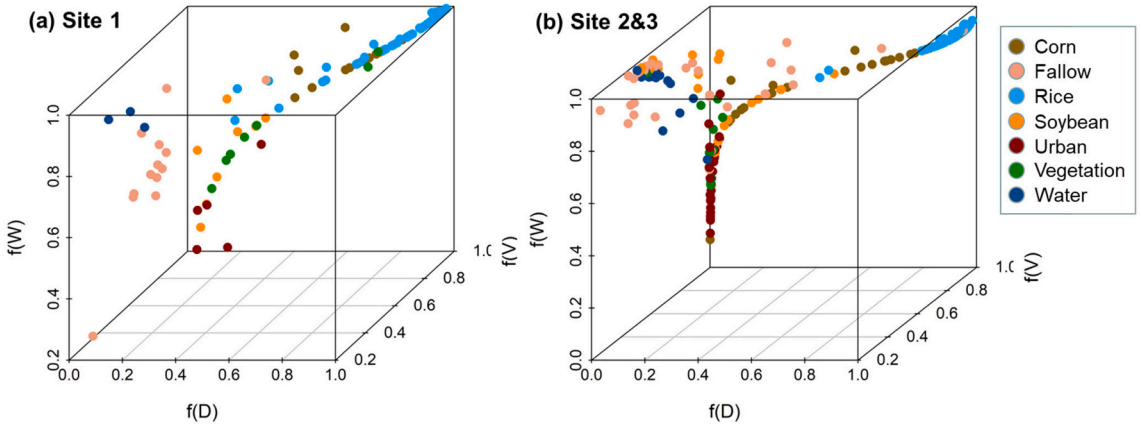

Fig. 13. 3D-axes plots of *f*(*D*), *f*(*W*), and *f*(*V*) values for different crops and land covers during the rice growth period at site 1 (a) and sites 2 and 3 (b).

features for rice field extraction (Dong and Xiao, 2016). This non-linear rescaling strategy can achieve a balance between omission and commission errors. Backscattering and phenological features during rice growth were widely employed by previous studies, such as the local minimum SAR backscattering intensity at the inundation phase (Clauss et al., 2018a; Nguyen et al., 2016; Son et al., 2021; Tian et al., 2018), dynamic backscatter range during growth (Clauss et al., 2018a; Nguyen et al., 2016; Nguyen and Wagner, 2017; Tian et al., 2018), and rice transplanting date (Li et al., 2020; Nguyen et al., 2016; Son et al., 2021; Zhan et al., 2021). These features showed a certain ability to distinguish between rice and non-rice fields (Fig. 14), but it is difficult to find a proper threshold for differentiating rice from other land covers from these features. Furthermore, the well-trained thresholds may not be applicable to different sites. For instance, the threshold used to filter out land parcels without inundation period in the method proposed by Clauss et al. (2018a, 2018b) was not applicable at sites 2 and 3 because lots of other crop fields also had minimum intensity lower than the threshold. Similarly, even if the precise phenology information is known, similar temporal profiles of SAR intensity would be observed for rice and other crops of the same period, resulting in a low UA based on phenology information such as the one proposed by Zhan et al. (2021). In this study, SPRI enlarges the index value difference between rice and non-rice covers, i.e., rice fields with a high value close to 1, and all non-rice fields with a low value close to 0, leading to a smaller intersection of rice and non-rice in the histogram of the SPRI value than the histogram of other original features (Fig. 14). The overlap of histograms of the SPRI value between rice and non-rice fields is small, demonstrating that a uniform threshold to separate rice and non-rice field by index segmentation is easy to determine for all sites.

6.2. *Transferability of the proposed method*

The robust performance among five sites demonstrates good transferability of the proposed method to different regions. Reasons for good transferability include (1) parameters determined locally and adaptively, (2) assistance of optical image, and (3) ease of separating rice and non-rice covers by index threshold.

First, the proposed method has two regional adaptive parameters, upper boundary "V line" (v) and lower boundary "W line" (w), catering for the differences of study sites in the geographical and climate background. The comparison between the method using local adaptive parameters and the unified parameter shows the contribution of the consideration of local environments to rice mapping (Fig. 15). Results from local parameters had significant increases in F1 score compared with that from unified parameters derived from the virtual large site (i.e., five sites combined as one site). The reason is that SAR backscatter values and their dynamic ranges vary under different situations, terrain conditions, rice cultivars and cultivation, and the incident angles in different regions (Chakraborty et al., 2005; Le Toan et al., 1997; Steele-Dunne et al., 2017). For instance, the incidence angle is one factor that influences the SAR backscattering intensity. Previous studies found that the radar backscatter decreases with the increase of incidence angle because of the attenuation of energy from double-bounce and multi-path scattering and possibly the increase in the specular reflectance of surface layers (Brisco et al., 1992; Xu et al., 2019). However, the incidence angle has the small range for each site covered by one Sentinel-1 tile. Therefore, the impact of the incidence angle on all pixels in one site can be considered as a systematic bias, and this bias can be mitigated by our designed index, which uses local adaptive parameters w and v to harmonize the difference among sites. Therefore, the strategy that SPRI parameters were collected from samples around target rice fields was able to eliminate the site differences. Furthermore, obtaining parameters from a large spatial extent would slightly reduce the classification accuracy, possibly attributed to the complex landscape within a large area (Fig. 16). As a result, we suggest dividing large areas into grids when applying our proposed method. Implementation of the proposed method in smaller grids (e.g., 0.5-degree grid) can acquire proper parameters which reflect the local land surface condition and thereby improve the classification accuracy.

Second, both parameters were determined automatically and adaptively with the assistance of Sentinel-2 images, which lifts the requirement of prior knowledge in other existing methods (Bazzi et al., 2019; Cai et al., 2019). Only vegetation index and water index of a certain percentile were used to determine the two parameters, v and w. We investigated the sensitivity of rice mapping accuracies to the selection of percentiles, which provides guidelines for users to apply the proposed methods to any other sites. Specifically, we selected different percentiles, namely, 5th, 10th, 25th, 50th, 75th, 90th and 95th percentile of the candidate backscattering intensity values described in Section 4.2, as the value of v and w to compute SPRI. F1 score of rice mapping at each site with combination of different v and w values was shown in Fig. 17. The result illustrates that the mapping accuracy is insensitive to the percentiles of both v and w at site 1 where paddy rice is the dominant crop. The F1 score is more sensitive to w than to v at the other four sites. However, Fig. 17 shows a large range of v and w values that can get a promising result in each site (e.g., F1 score > 0.8), suggesting the ease for users to select suitable percentiles for end users. Specifically, we recommend 10th to 25th percentile for determining v value in any landscapes, because paddy rice often has a relatively lower backscatter than other vegetation and crops. For w value, we suggest 5th to 25th percentiles for flat landscapes (e.g., the three USA sites) and 75th to 95th percentiles for hilly landscapes (e.g., the two Chinese sites). Hilly areas often have water bodies which are deeper than the flooded stage of paddy fields. Given that C-band backscatter is negatively correlated to

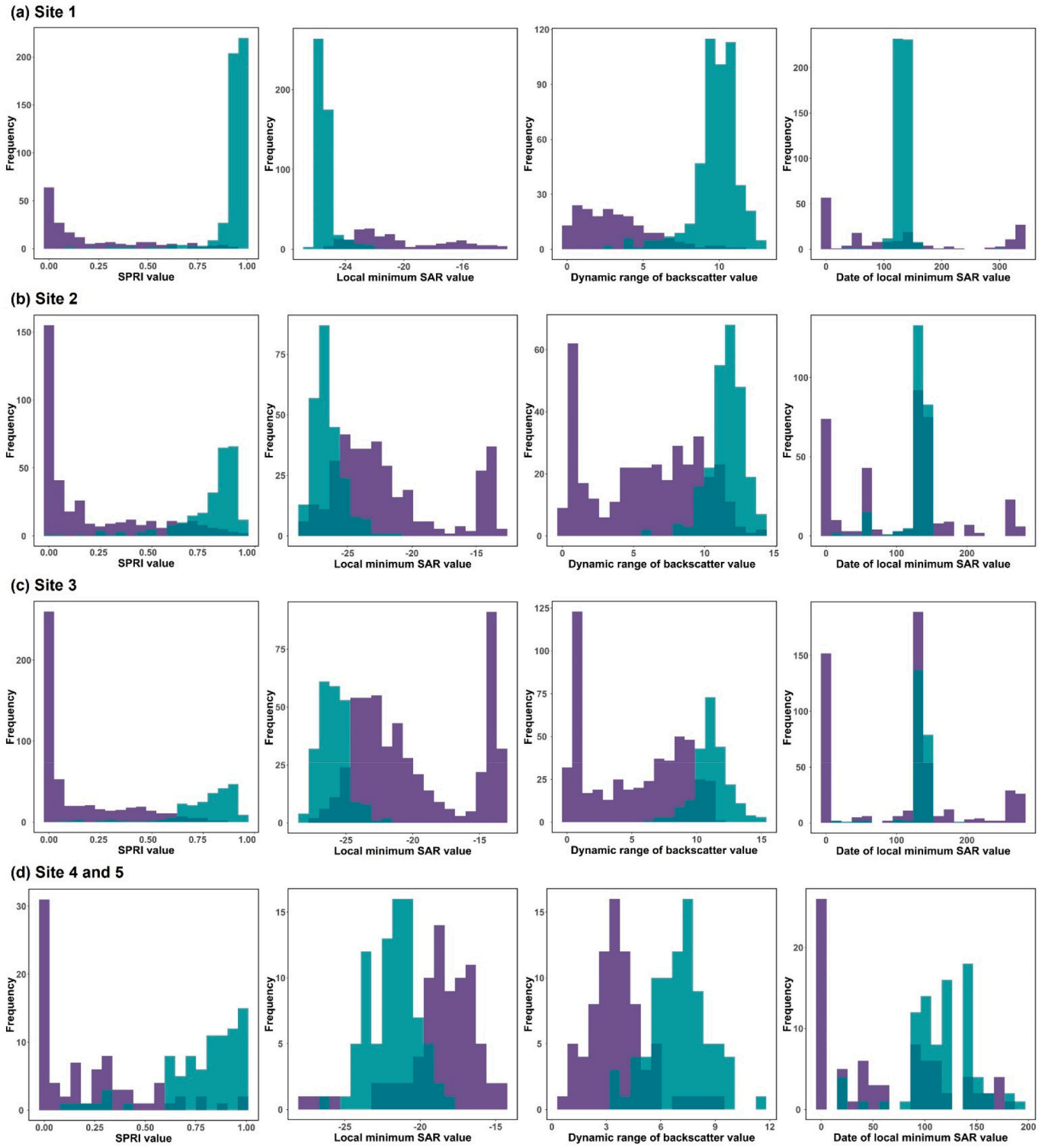

Fig. 14. The histograms of SPRI value, local minimum backscattering intensity during transplanting stage, dynamic backscatter range and transplanting date detected from rice (green bar) and non-rice (purple bar) validation samples for site 1 (a), site 2 (b), site 3 (c), and site 4 & 5 (d). (For interpretation of the references to color in this figure legend, the reader is referred to the web version of this article.)

water depth (Kasischke et al., 2009), a higher percentile (e.g., 75th to 95th) can ensure that the parameter w represents the backscatter of the flooded stage of rice paddies.

The validity of recommended percentiles was verified in an extra site (111°27′36″-111°34′48″E, 28°58′12″-29°4′12”N) in Taoyuan county, Hunan Province, China, which has flat terrain. Single-season rice (middle rice) and double-season rice (early and late rice) are grown in this site. The middle rice is transplanted at the late May and harvested at the late August, while the early and late rice are transplanted at the late April and late July respectively. We collected 123 samples containing the single-season rice, double-season rice and non-rice land cover through field work. All mapping procedures are consistent with other

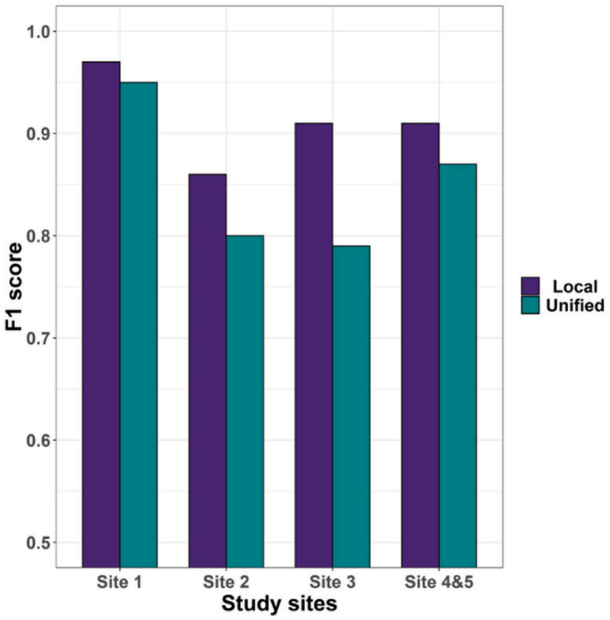

Fig. 15. Comparison of the rice mapping accuracy (F1 score) between the proposed method using local adaptive parameters and the unified parameter for all sites.

five sites. The algorithm parameters used for Taoyuan site are consistent with those of the American sites because all of them are flat areas. The mapping results and accuracy assessment are shown in Fig. 18 and Table 6. The SPRI method also performed well for separating rice and non-rice fields in Taoyuan county, with the overall accuracy 0.92, implying that the strategy of determining *v* and *w* percentile based on terrain conditions is effective.

Lastly, the determination of a threshold for separating rice and non-rice covers from SPRI is relatively easy because SPRI effectively balanced between the commission error and omission error and eliminated the site difference. The receiver operating characteristic (ROC) curve as shown in Fig. 19 (a) proved that our proposed index is insensitive to the site differences, with the Area under the Curve of ROC (AUC ROC) ranging from 0.92 to 0.98, which demonstrates the good separability for rice and non-rice (Bradley, 1997). Therefore, the binary-classification threshold for mapping rice fields from SPRI which is the only empirical parameter in the proposed method is easy to determine. This threshold can be determined based on the user demand, depending on whether the user is more concerned about omission error or commission error. In general, the UA increases with the threshold, while the PA drops with the threshold. Our result at five sites suggested that any value in the range of 0.5–0.7 can produce a satisfying rice map by balancing the UA and PA (Fig. 19 (b)). We also suggest two alternative ways to determine the threshold. First, users can use any supervised classifiers, such as SVM and MLC, to classify SPRI image if they have collected some ground samples. Second, unsupervised classifiers, such as K-means and ISODATA, can be used to divide SPRI images into two classes.

6.3. Applicable conditions and limitations

First, the proposed method does not need dense cloud-free Sentinel-2 images which makes it very helpful to map paddy rice in cloudy regions, but it requires at least one cloud-free Sentinel-2 image as auxiliary data to obtain cropland objects by segmentation and help determine the parameter values. However, this requirement can be lifted for extreme cases when no cloud-free Sentinel-2 images exist. In such a case, any land cover products can be used to determine the cropland objects and the adaptive parameters. Furthermore, SAR time series is an alternative to conduct image segmentations, which is also used by previous studies (Qi et al., 2012; Wang et al., 2018; Zhang et al., 2021).

Second, the proposed method does not require the ground truth sample. Data-driven methods (e.g., deep learning) can extract informative features from input data and produce promising results, which are important for agriculture management and precise agriculture. However, the requirement of training samples challenges the transferability of deep learning-based methods. For instance, the compared deep learning method proposed by Yang et al. (2022) received satisfied results in sites 1–3 where there are abundant training samples from CDL datasets, but the mapping accuracy decreased a lot in two Chinese sites because of the lack of ground samples to tune the model. Therefore, our work aims to map paddy rice from a different way, i.e., an index without ground samples, which could be valuable supplementary to the family of paddy rice mapping methods. The performance of SPRI in rice mapping can also be improved if samples over the new site are available, since they can help determine the threshold for separating rice and non-rice covers.

Third, the proposed method is capable of mapping rice fields and rice cropping intensities in regions where single-season rice and double-

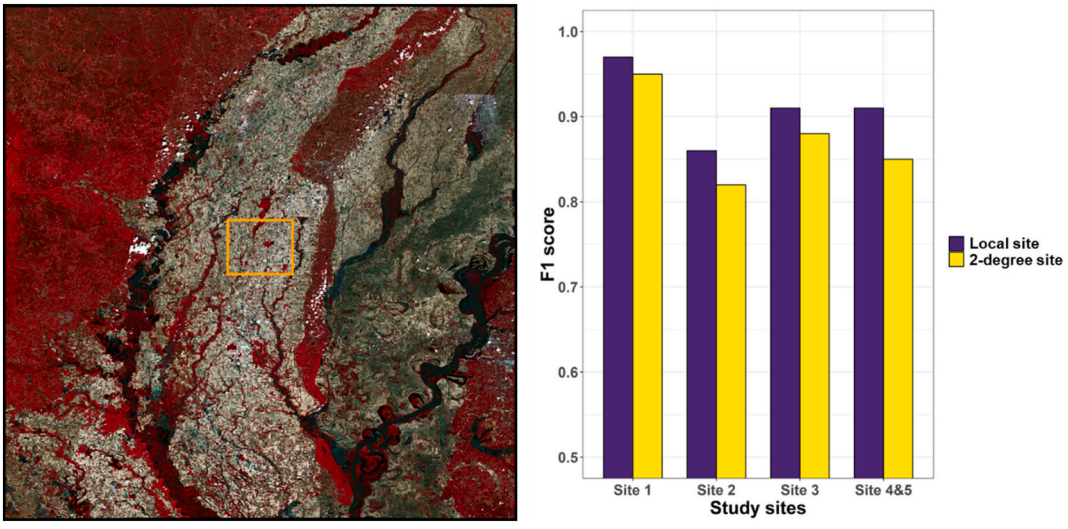

Fig. 16. Comparison of the rice mapping accuracy (F1 score) between the proposed method using parameters obtained from the local site (highlighted by orange rectangular) and from 2-degree site (the whole region).

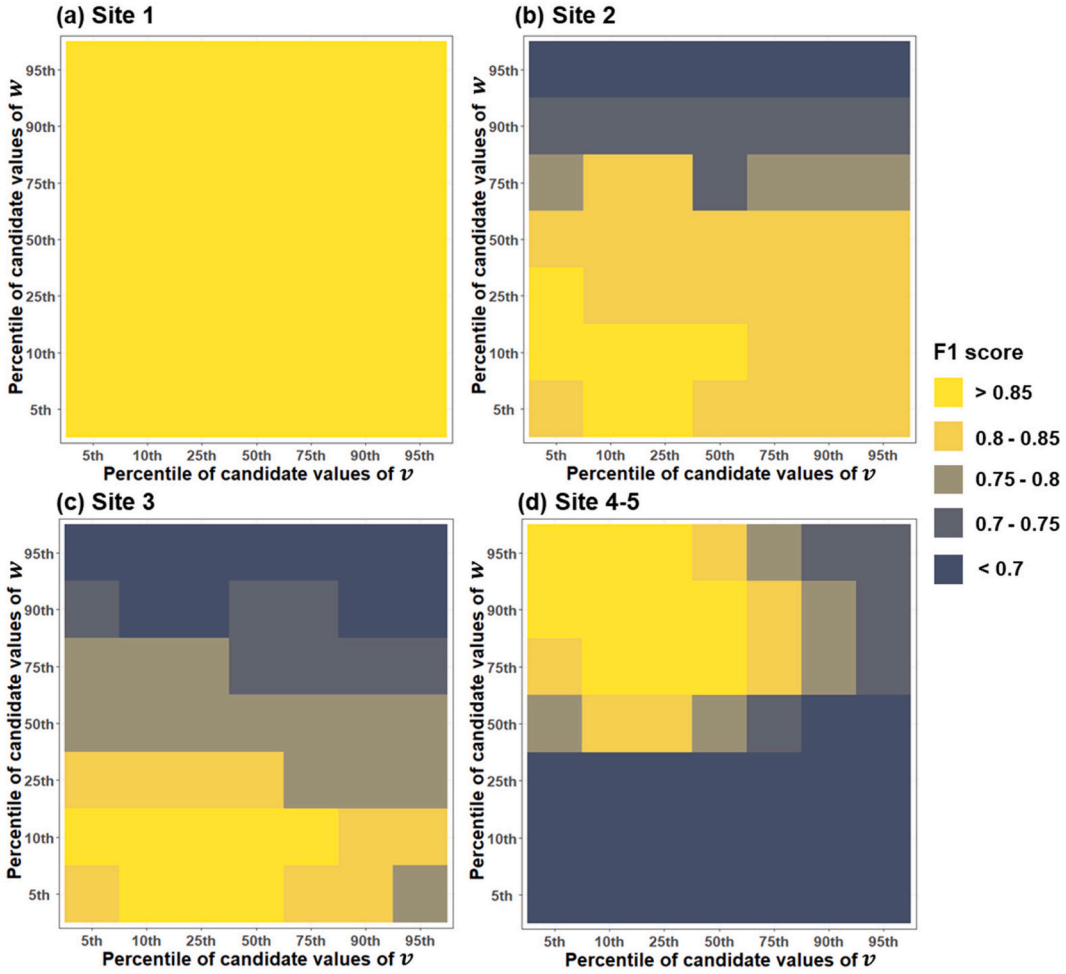

Fig. 17. The F1 score under combinations of different V and W line values in sites 1–3 in the plain area (a-c), and sites 4–5 in the hilly area (d).

season rice concurrently exist (see Fig. 18(b)). SPRI received satisfactory overall accuracy of 0.86 for mapping the single-season and double-season rice in Taoyuan County (Table 6). Previous studies demonstrated that the late rice also exhibited the similar "V"-shape pattern with the early rice during the growth period (Zhan et al., 2021). Such "V"-shape pattern also implies that the late rice has the similar backscattering mechanism during the growth period (Fig. 18 (d)). Since our proposed SPRI method considers the backscattering dynamic characteristics of rice growth, the algorithm is theoretically applicable in regions where double rice is grown. However, the omission error of double rice mapping was higher than that of single rice mapping. The possible reason is that the inundation period of late rice is shorter than that of early and middle rice, so the inundation period of late rice may not be observed from the SAR images with a 12-day revisit cycle. To tackle this problem, increasing the frequency of observations to capture the inundation period of late rice by combining the same or different orbit data is a possible solution. Our proposed method may also misclassify little amount of water-intensive crop parcels as rice (e.g., commission errors caused by soybean and fallow land in sites 2–3) when the similar "V"-shape pattern exists during their growth period. Additional knowledge such as the planting date and length of growth may further alleviate this problem. In addition, in the northern region where the snow and ice melting in Spring can greatly decrease the SAR backscatters, we suggest applying our proposed method to the SAR time series from the season without snow and ice melting, which is long enough to cover a paddy rice cycle.

7. Conclusion

In this study, we designed a new SAR-based paddy rice mapping index, called SPRI, to distinguish the rice field from other land cover types and crops based on Sentinel-1 time series data. Sentinel-2 images were used as axillary data to estimate the parameters in SPRI. We tested its capacity and robustness in five sites that are different in climate, terrain and cropping regimes and compared its performance with three existing methods. Results show that the SPRI was able to provide an accurate classification map with an overall accuracy of over 88% and an F1 score of over 0.86 at all sites, which is better than the existing methods. The proposed SPRI based rice mapping method has several advantages: (1) it does not need any prior knowledge (e.g., phenology information) or reference samples; (2) it does not have many predefined parameters; (3) it normalizes site differences to a large extent; and (4) it can balance the commission and omission errors. Therefore, the proposed method has high flexibility and applicability to support paddy rice mapping in large areas, especially for cloudy regions where optical remote sensing data are limited.

CRediT authorship contribution statement

Shuai Xu: Methodology, Software, Formal analysis, Investigation, Writing – original draft, Writing – review & editing, Visualization. **Xiaolin Zhu:** Conceptualization, Methodology, Supervision, Resources, Writing – original draft, Writing – review & editing, Project administration, Funding acquisition. **Jin Chen:** Conceptualization, Methodology, Writing – review & editing. **Xuelin Zhu:** Resources, Visualization,

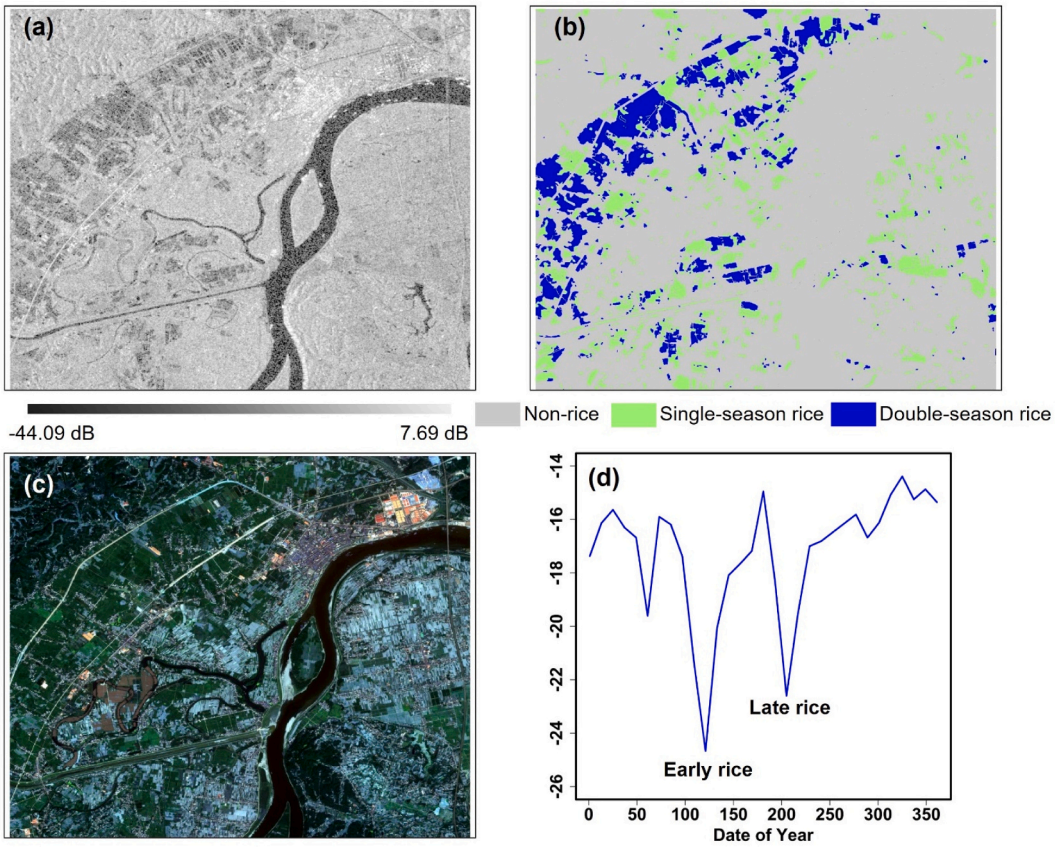

Fig. 18. Rice mapping in the Taoyuan site: backscattering intensity of VH band at the inundation period of late rice (a), objected-based rice cropping intensity map derived from SPRI (b), the true-color composite of Sentinel-2 image (c), and example of the temporal pattern of double-season rice during the whole year (d).

Table 6
Confusion matrix of rice mapping result for Taoyuan site.

		Reference		
		Single rice	Double rice	Non-rice
Mapping result	Single rice	25	6	2
	Double rice	0	29	0
	Non-rice	4	4	53

Writing – review & editing. **Mingjie Duan:** Resources, Visualization, Writing – review & editing. **Bingwen Qiu:** Investigation, Writing – review & editing. **Luoma Wan:** Investigation, Writing – review & editing. **Xiaoyue Tan:** Investigation, Writing – review & editing. **Yi Nam Xu:** Investigation, Writing – review & editing. **Ruyin Cao:** Writing – review & editing, Funding acquisition.

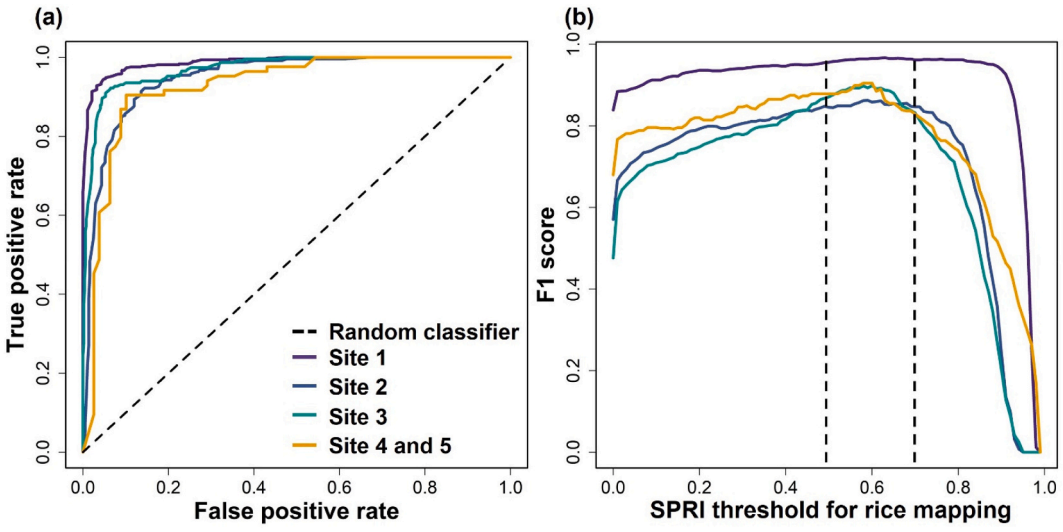

Fig. 19. ROC curve for all sites (a) and sensitivity analysis of SPRI binary-classification threshold for all sites (b).

Declaration of Competing Interest

The authors declare that they have no known competing financial interests or personal relationships that could have appeared to influence the work reported in this paper.

Data availability

Data will be made available on request.

Acknowledgments

This study was supported by the National Natural Science Foundation of China (project No.42022060), the Sichuan Science and Technology Program (project No.2022YFH0106), and the Hong Kong Polytechnic University (project Nos. ZVN6 and ZVVF). We thank Prof. Shihua Li from the University of Electronic Science and Technology of China for providing field samples for validation.

Appendix A. Supplementary data

Supplementary data to this article can be found online at https://doi.org/10.1016/j.rse.2022.113374.

References

Adrian, J., Sagan, V., Maimaitijiang, M., 2021. Sentinel SAR-optical fusion for crop type mapping using deep learning and Google earth engine. ISPRS J. Photogramm. Remote Sens. 175 (August 2020), 215–235. https://doi.org/10.1016/j.isprsjprs.2021.02.018.

Asilo, S., De Bie, K., Skidmore, A., Nelson, A., Barbieri, M., Maunahan, A., 2014. Complementarity of two rice mapping approaches: characterizing strata mapped by hypertemporal MODIS and rice paddy identification using multitemporal SAR. Remote Sens. 6 (12), 12789–12814. https://doi.org/10.3390/rs61212789.

Bazzi, H., Baghdadi, N., El Hajj, M., Zribi, M., Minh, D.H.T., Ndikumana, E., Courault, D., Belhouchette, H., 2019. Mapping paddy rice using Sentinel-1 SAR time series in Camargue, France. Remote Sens. 11 (7), 887. https://doi.org/10.3390/rs11070887.

Bian, J., Li, A., Lei, G., Zhang, Z., Nan, X., 2020. Global high-resolution mountain green cover index mapping based on landsat images and Google earth engine. ISPRS J. Photogramm. Remote Sens. 162, 63–76.

Bleau, A., Leon, L.J., 2000. Watershed-based segmentation and region merging. Comput. Vis. Image Underst. 77 (3), 317–370. https://doi.org/10.1006/cviu.1999.0822.

Boryan, C., Yang, Z., Mueller, R., Craig, M., 2011. Monitoring US agriculture: the US department of agriculture, national agricultural statistics service, cropland data layer program. Geocarto Int. 26 (5), 341–358. Monitoring US agriculture: the US department of agriculture, national agricultural statistics service, cropland data layer program.

Bradley, A.P., 1997. The use of the area under the ROC curve in the evaluation of machine learning algorithms. Pattern Recogn. 30 (7), 1145–1159. https://doi.org/10.1016/S0031-3203(96)00142-2.

Brisco, B., Brown, R.J., Gairns, J.G., Snider, B., 1992. Temporal ground-based scatterometer observations of crops in Western Canada. Can. J. Remote. Sens. 18 (1), 14–21. https://doi.org/10.1080/07038992.1992.10855138.

Cai, Y., Lin, H., Zhang, M., 2019. Mapping paddy rice by the object-based random forest method using time series Sentinel-1/Sentinel-2 data. Adv. Space Res. 64 (11), 2233–2244. https://doi.org/10.1016/j.asr.2019.08.042.

Canisius, F., Shang, J., Liu, J., Huang, X., Ma, B., Jiao, X., Geng, X., Kovacs, J.M., Walters, D., 2018. Tracking crop phenological development using multi-temporal polarimetric Radarsat-2 data. Remote Sens. Environ. 210, 508–518. https://doi.org/10.1016/j.rse.2017.07.031.

Chakraborty, M., Manjunath, K.R., Panigrahy, S., Kundu, N., Parihar, J.S., 2005. Rice crop parameter retrieval using multi-temporal, multi-incidence angle Radarsat SAR data. ISPRS J. Photogramm. Remote Sens. 59 (5), 310–322. https://doi.org/10.1016/j.isprsjprs.2005.05.001.

Chauhan, S., Darvishzadeh, R., Boschetti, M., Pepe, M., Nelson, A., 2019. Remote sensing-based crop lodging assessment: current status and perspectives. ISPRS J. Photogramm. Remote Sens. 151, 124–140. https://doi.org/10.1016/j.isprsjprs.2019.03.005.

Chen, J., Zhang, M., Wang, L., Shimazaki, H., Tamura, M., 2005. A new index for mapping lichen-dominated biological soil crusts in desert areas. Remote Sens. Environ. 96 (2), 165–175. https://doi.org/10.1016/j.rse.2005.02.011.

Chen, J., Han, Y., Zhang, J., 2014. Mapping rice crop fields using C band polarimetric SAR data. In: 2014 The 3rd International Conference on Agro-Geoinformatics, Agro-Geoinformatics 2014, pp. 1–4. https://doi.org/10.1109/Agro-Geoinformatics.2014.6910675.

Chen, J., Lin, H., Pei, Z., 2007. Application of ENVISAT ASAR data in mapping rice crop growth in southern China. IEEE Geosci. Remote Sens. Lett. 4 (3), 431–435. https://doi.org/10.1109/LGRS.2007.896996.

Clauss, K., Ottinger, M., Künzer, C., 2018. Mapping rice areas with Sentinel-1 time series and superpixel segmentation. Int. J. Remote Sens. 39 (5), 1399–1420. https://doi.org/10.1080/01431161.2017.1404162.

Clauss, K., Ottinger, M., Leinenkugel, P., Kuenzer, C., 2018. Estimating rice production in the Mekong Delta, Vietnam, utilizing time series of Sentinel-1 SAR data. Int. J. Appl. Earth Obs. Geoinf. 73 (July), 574–585. https://doi.org/10.1016/j.jag.2018.07.022.

Dan, C.A.O., Feng, J., Bai, L., Lan, X.U.N., Jiubg, H., Sun, J., Zhang, J., 2021. Delineating the rice crop activities in Northeast China through regional parametric synthesis using satellite remote sensing time-series data from 2000 to 2015. J. Integr. Agric. 20 (2), 424–437. https://doi.org/10.1016/S2095-3119(20)63458-X.

De Castro, A.I., Torres-Sánchez, J., Peña, J.M., Jiménez-Brenes, F.M., Csillik, O., López-Granados, F., 2018. An automatic random forest-OBIA algorithm for early weed mapping between and within crop rows using UAV imagery. Remote Sens. 10 (2), 285. https://doi.org/10.3390/rs10020285.

Diao, C., Yang, Z., Gao, F., Zhang, X., Yang, Z., 2021. Hybrid phenology matching model for robust crop phenological retrieval. ISPRS J. Photogramm. Remote Sens. 181, 308–326. https://doi.org/10.1016/j.isprsjprs.2021.09.011.

Dong, J., Xiao, X., 2016. Evolution of regional to global paddy rice mapping methods: a review. ISPRS J. Photogramm. Remote Sens. 119, 214–227. https://doi.org/10.1016/j.isprsjprs.2016.05.010.

Dong, J., Xiao, X., Menarguez, M.A., Zhang, G., Qin, Y., Thau, D., Biradar, C., Moore III, B., 2016. Mapping paddy rice planting area in northeastern Asia with landsat 8 images, phenology-based algorithm and Google earth engine. Remote Sens. Environ. 185, 142–154. https://doi.org/10.1016/j.rse.2016.02.016.

Fiorillo, E., Di Giuseppe, E., Fontanelli, G., Maselli, F., 2020. Lowland rice mapping in Sédhiou region (Senegal) using sentinel 1 and sentinel 2 data and random forest. Remote Sens. 12 (20), 3403. https://doi.org/10.3390/rs12203403.

Food, O.L., 1994. Agriculture Organisation of the United Nations. In: Food and Agriculture Organisation Statistical Series Volume 46. Food and Agriculture Organisation of the United Nations.

Gao, H., Wang, C., Wang, G., Fu, H., Zhu, J., 2021. A novel crop classification method based on ppfSVM classifier with time-series alignment kernel from dual-polarization SAR datasets. Remote Sens. Environ. 264, 112628 https://doi.org/10.1016/j.rse.2021.112628.

He, Z., Li, S., Wang, Y., Dai, L., Lin, S., 2018. Monitoring rice phenology based on backscattering characteristics of multi-temporal RADARSAT-2 datasets. Remote Sens. 10 (2) https://doi.org/10.3390/rs10020340.

Hripcsak, G., Rothschild, A.S., 2005. Agreement, the F-measure, and reliability in information retrieval. J. Am. Med. Inform. Assoc. 12 (3), 296–298. https://doi.org/10.1197/jamia.M1733.

Inoue, Y., Sakaiya, E., Wang, C., 2014. Capability of C-band backscattering coefficients from high-resolution satellite SAR sensors to assess biophysical variables in paddy rice. Remote Sens. Environ. 140, 257–266. https://doi.org/10.1016/j.rse.2013.09.001.

Jenks, G.F., 1967. The data model concept in statistical mapping. In: International Yearbook of Cartography, 7, pp. 186–190.

Jiao, X., Kovacs, J.M., Shang, J., McNairn, H., Walters, D., Ma, B., Geng, X., 2014. Object-oriented crop mapping and monitoring using multi-temporal polarimetric RADARSAT-2 data. ISPRS J. Photogramm. Remote Sens. 96, 38–46. https://doi.org/10.1016/j.isprsjprs.2014.06.014.

Johnson, D.M., Mueller, R., 2010. The 2009 cropland data layer. Photogramm. Eng. Remote Sens 76 (11), 1201–1205.

Johnson, D.M., Mueller, R., 2021. Pre-and within-season crop type classification trained with archival land cover information. Remote Sens. Environ. 264, 112576 https://doi.org/10.1016/j.rse.2021.112576.

Kasischke, E.S., Bourgeau-Chavez, L.L., Rober, A.R., Wyatt, K.H., Waddington, J.M., Turetsky, M.R., 2009. Effects of soil moisture and water depth on ERS SAR backscatter measurements from an Alaskan wetland complex. Remote Sens. Environ. 113, 1868–1873.

Le Toan, T., Ribbes, F., Wang, L.-F., Floury, N., Ding, K.-H., Kong, J.A., Fujita, M., Kurosu, T., 1997. Rice crop mapping and monitoring using ERS-1 data based on experiment and modeling results. IEEE Trans. Geosci. Remote Sens. 35 (1), 41–56. https://doi.org/10.1109/36.551933.

Lebourgeois, V., Dupuy, S., Vintrou, É., Ameline, M., Butler, S., Bégué, A., 2017. A combined random forest and OBIA classification scheme for mapping smallholder agriculture at different nomenclature levels using multisource data (simulated Sentinel-2 time series, VHRS and DEM). Remote Sens. 9 (3), 259. https://doi.org/10.3390/rs9030259.

Li, H., Fu, D., Huang, C., Su, F., Liu, Q., Liu, G., Wu, S., 2020. An approach to high-resolution rice paddy mapping using time-series sentinel-1 Sar data in the mun river basin, Thailand. Remote Sensing 12 (23), 1–19. https://doi.org/10.3390/rs12233959.

Li, K., Brisco, B., Yun, S., Touzi, R., 2012. Polarimetric decomposition with RADARSAT-2 for rice mapping and monitoring. Can. J. Remote. Sens. 38 (2), 169–179. https://doi.org/10.5589/m12-024.

Lee, J. Sen., Grunes, M.R., Grandi, G. de., 1999. Polarimetric SAR speckle filtering and its implication for classification. IEEE Trans. Geosci. Remote Sens. 37 (5), 2363–2373. https://doi.org/10.1109/36.789635.

Li, M., Bijker, W., 2019. Vegetable classification in Indonesia using dynamic time warping of sentinel-1A dual polarization SAR time series. Int. J. Appl. Earth Obs. Geoinf. 78, 268–280. https://doi.org/10.1016/j.jag.2019.01.009.

Li, Q., Wang, C., Zhang, B., Lu, L., 2015. Object-based crop classification with landsat-MODIS enhanced time-series data. Remote Sens. 7 (12), 16091–16107. https://doi.org/10.3390/rs71215820.

Lin, Z., Zhong, R., Xiong, X., Guo, C., Xu, J., Zhu, Y., Xu, J., Ying, Y., Ting, K.C., Huang, J., Lin, T., 2022. Large-scale Rice mapping using multi-task spatiotemporal

deep learning and Sentinel-1 SAR time series. Remote Sens. 14 (3) https://doi.org/10.3390/rs14030699.
Lowder, S.K., Skoet, J., Raney, T., 2016. The number, size, and distribution of farms, smallholder farms, and family farms worldwide. World Dev. 87, 16–29. https://doi.org/10.1016/j.worlddev.2015.10.041.
McFeeters, S.K., 2013. Using the normalized difference water index (NDWI) within a geographic information system to detect swimming pools for mosquito abatement: a practical approach. Remote Sens. 5 (7), 3544–3561. https://doi.org/10.3390/rs5073544.
Montzka, S.A., Dlugokencky, E.J., Butler, J.H., 2011. Non-CO 2 greenhouse gases and climate change. Nature 476 (7358), 43–50. https://doi.org/10.1038/nature10322.
Motohka, T., Nasahara, K.N., Miyata, A., Mano, M., Tsuchida, S., 2009. Evaluation of optical satellite remote sensing for rice paddy phenology in monsoon Asia using a continuous in situ dataset. Int. J. Remote Sens. 30 (17), 4343–4357. https://doi.org/10.1080/01431160802549369.
Nguyen, D.B., Gruber, A., Wagner, W., 2016. Mapping rice extent and cropping scheme in the Mekong Delta using sentinel-1A data. Remote Sens. Lett. 7 (12), 1209–1218. https://doi.org/10.1080/2150704X.2016.1225172.
Nguyen, D.B., Wagner, W., 2017. European rice cropland mapping with Sentinel-1 data: the Mediterranean region case study. Water 9 (6), 392. https://doi.org/10.3390/w9060392.
Pan, B., Zheng, Y., Shen, R., Ye, T., Zhao, W., Dong, J., Ma, H., Yuan, W., 2021. High resolution distribution dataset of double-season paddy rice in China. Remote Sens. 13 (22) https://doi.org/10.3390/rs13224609.
Park, S., Im, J., Park, S., Yoo, C., Han, H., Rhee, J., 2018. Classification and mapping of paddy rice by combining landsat and SAR time series data. Remote Sens. 10 (3), 1–22. https://doi.org/10.3390/rs10030447.
Peña-Barragán, J.M., Ngugi, M.K., Plant, R.E., Six, J., 2011. Object-based crop identification using multiple vegetation indices, textural features and crop phenology. Remote Sens. Environ. 115 (6), 1301–1316. https://doi.org/10.1016/j.rse.2011.01.009.
Peng, W., Kuang, T., Tao, S., 2019. Quantifying influences of natural factors on vegetation NDVI changes based on geographical detector in Sichuan, western China. J. Clean. Prod. 233, 353–367. https://doi.org/10.1016/j.jclepro.2019.05.355.
Qi, Z., Yeh, A.G.-O., Li, X., 2017. A crop phenology knowledge-based approach for monthly monitoring of construction land expansion using polarimetric synthetic aperture radar imagery. ISPRS J. Photogramm. Remote Sens. 133, 1–17. https://doi.org/10.1016/j.isprsjprs.2017.09.009.
Qi, Z., Yeh, A.G.-O., Li, X., Lin, Z., 2012. A novel algorithm for land use and land cover classification using RADARSAT-2 polarimetric SAR data. Remote Sens. Environ. 118, 21–39. https://doi.org/10.1016/j.rse.2011.11.001.
Qiu, B., Li, W., Tang, Z., Chen, C., Qi, W., 2015. Mapping paddy rice areas based on vegetation phenology and surface moisture conditions. Ecol. Indic. 56, 79–86. https://doi.org/10.1016/j.ecolind.2015.03.039.
Shafarenko, L., Petrou, M., Kittler, J., 1997. Automatic watershed segmentation of randomly textured color Images. IEEE Trans. Image Process. 6 (11), 1530–1544. https://doi.org/10.1109/83.641413.
Shah Hosseini, R., Entezari, I., Homayouni, S., Motagh, M., Mansouri, B., 2011. Classification of polarimetric SAR images using support vector machines. Can. J. Remote. Sens. 37 (2), 220–233. https://doi.org/10.5589/m11-029.
Son, N.-T., Chen, C.-F., Chen, C.-R., Toscano, P., Cheng, Y.-S., Guo, H.-Y., Syu, C.-H., 2021. A phenological object-based approach for rice crop classification using time-series Sentinel-1 synthetic aperture radar (SAR) data in Taiwan. Int. J. Remote Sens. 42 (7), 2722–2739. https://doi.org/10.1080/01431161.2020.1862440.
Steele-Dunne, S.C., McNairn, H., Monsivais-Huertero, A., Judge, J., Liu, P.-W., Papathanassiou, K., 2017. Radar remote sensing of agricultural canopies: a review. IEEE J. Sel. Top. Appl. Earth Obs. Remote Sens. 10 (5), 2249–2273. https://doi.org/10.1109/JSTARS.2016.2639043.
Sulik, J.J., Long, D.S., 2016. Spectral considerations for modeling yield of canola. Remote Sens. Environ. 184, 161–174. https://doi.org/10.1016/j.rse.2016.06.016.
Thorp, K.R., Drajat, D., 2021. Deep machine learning with Sentinel satellite data to map paddy rice production stages across West Java, Indonesia. Remote Sens. Environ. 265 (September), 112679 https://doi.org/10.1016/j.rse.2021.112679.
Tian, H., Wu, M., Wang, L., Niu, Z., 2018. Mapping early, middle and late rice extent using sentinel-1A and Landsat-8 data in the Poyang lake plain, China. Sensors 18 (1), 185. https://doi.org/10.3390/s18010185.
Tian, H., Lu, C., Ciais, P., Michalak, A.M., Canadell, J.G., Saikawa, E., Huntzinger, D.N., Gurney, K.R., Sitch, S., Zhang, B., 2016. The terrestrial biosphere as a net source of greenhouse gases to the atmosphere. Nature 531 (7593), 225–228. https://doi.org/10.1038/nature16946.
Torbick, N., Chowdhury, D., Salas, W., Qi, J., 2017. Monitoring rice agriculture across Myanmar using time series Sentinel-1 assisted by Landsat-8 and PALSAR-2. Remote Sens. 9 (2), 119. https://doi.org/10.3390/rs9020119.
Tornos, L., Huesca, M., Dominguez, J.A., Moyano, M.C., Cicuendez, V., Recuero, L., Palacios-Orueta, A., 2015. Assessment of MODIS spectral indices for determining rice paddy agricultural practices and hydroperiod. ISPRS J. Photogramm. Remote Sens. 101, 110–124. https://doi.org/10.1016/j.isprsjprs.2014.12.006.
Wang, L., Marzahn, P., Bernier, M., Ludwig, R., 2018. Mapping permafrost landscape features using object-based image classification of multi-temporal SAR images. ISPRS J. Photogramm. Remote Sens. 141, 10–29. https://doi.org/10.1016/j.isprsjprs.2018.03.026.
Watkins, B., van Niekerk, A., 2019. A comparison of object-based image analysis approaches for field boundary delineation using multi-temporal Sentinel-2 imagery. Comput. Electron. Agric. 158 (February), 294–302. https://doi.org/10.1016/j.compag.2019.02.009.
Watkins, B., Van Niekerk, A., 2019. Automating field boundary delineation with multi-temporal Sentinel-2 imagery. Comput. Electron. Agric. 167 (October), 105078 https://doi.org/10.1016/j.compag.2019.105078.
Wei, P., Chai, D., Huang, R., Peng, D., Lin, T., Sha, J., Sun, W., Huang, J., 2022. Rice mapping based on Sentinel-1 images using the coupling of prior knowledge and deep semantic segmentation network: a case study in Northeast China from 2019 to 2021. Int. J. Appl. Earth Obs. Geoinf. 112 (August), 102948 https://doi.org/10.1016/j.jag.2022.102948.
Wei, P., Chai, D., Lin, T., Tang, C., Du, M., Huang, J., 2021. Large-scale rice mapping under different years based on time-series Sentinel-1 images using deep semantic segmentation model. ISPRS J. Photogramm. Remote Sens. 174 (September 2020), 198–214. https://doi.org/10.1016/j.isprsjprs.2021.02.011.
Weiss, M., Jacob, F., Duveiller, G., 2020. Remote sensing for agricultural applications: a meta-review. Remote Sens. Environ. 236, 111402 https://doi.org/10.1016/j.rse.2019.111402.
Wu, X., Xiao, X., Steiner, J., Yang, Z., Qin, Y., Wang, J., 2021. Spatiotemporal changes of winter wheat planted and harvested areas, photosynthesis and grain production in the contiguous United States from 2008–2018. Remote Sens. 13 (9), 1735. https://doi.org/10.3390/rs13091735.
Xiao, X., Boles, S., Frolking, S., Salas, W., Moore Iii, B., Li, C., He, L., Zhao, R., 2002. Observation of flooding and rice transplanting of paddy rice fields at the site to landscape scales in China using VEGETATION sensor data. Int. J. Remote Sens. 23 (15), 3009–3022. https://doi.org/10.1080/01431160110107734.
Xie, L., Zhang, H., Wu, F., Wang, C., Zhang, B., 2015. Capability of rice mapping using hybrid polarimetric SAR data. IEEE J. Sel. Top. Appl. Earth Obs. Remote Sens. 8 (8), 3812–3822. https://doi.org/10.1109/JSTARS.2014.2387214.
Xu, L., Zhang, H., Wang, C., Wei, S., Zhang, B., Wu, F., Tang, Y., 2021. Paddy rice mapping in Thailand using time-series sentinel-1 data and deep learning model. Remote Sens. 13 (19) https://doi.org/10.3390/rs13193994.
Xu, S., Qi, Z., Li, X., Yeh, A.G.-O., 2019. Investigation of the effect of the incidence angle on land cover classification using fully polarimetric SAR images. Int. J. Remote Sens. 40 (4), 1576–1593. https://doi.org/10.1080/01431161.2018.1528021.
Yang, H., Pan, B., Wu, W., Tai, J., 2018. Field-based rice classification in wuhua county through integration of multi-temporal sentinel-1A and Landsat-8 OLI data. Int. J. Appl. Earth Obs. Geoinf. 69, 226–236. https://doi.org/10.1016/j.jag.2018.02.019.
Yang, L., Huang, R., Huang, J., Lin, T., Wang, L., Mijiti, R., Wei, P., Tang, C., Shao, J., Li, Q., Du, X., 2022. Semantic segmentation based on temporal features: learning of temporal-spatial information from time-series SAR images for Paddy Rice mapping. IEEE Trans. Geosci. Remote Sens. 60 https://doi.org/10.1109/TGRS.2021.3099522.
Zhan, P., Zhu, W., Li, N., 2021. An automated rice mapping method based on flooding signals in synthetic aperture radar time series. Remote Sens. Environ. 252, 112112 https://doi.org/10.1016/j.rse.2020.112112.
Zhang, X., Chan, N.W., Pan, B., Ge, X., Yang, H., 2021. Mapping flood by the object-based method using backscattering coefficient and interference coherence of Sentinel-1 time series. Sci. Total Environ. 794, 148388 https://doi.org/10.1016/j.scitotenv.2021.148388.
Zhu, X.L., Li, Q., Shen, M.G., Chen, J., Wu, J., 2008. A methodology for multiple cropping index extraction based on NDVI time-series. J. Nat. Resour. 23, 534–544.